A global wave parameter database for geophysical applications. Part 3: improved forcing and spectral resolution

Matias Alday[a], Mickael Accensi[a], Fabrice Ardhuin[a,b], Guillaume Dodet[a]

[a] *Univ. Brest, CNRS, Ifremer, IRD, Laboratoire d'Océanographie Physique et Spatiale, Brest, France*

[b] *Scripps Institution of Oceanography, University of California San Diego, La Jolla, California*

Abstract

Numerical wave models are used for a wide range of applications, from the global ocean to coastal scales. Here we report on significant improvements compared to the previous hindcast detailed in Part 2 of the present study by Rascle and Ardhuin (2013). This result was obtained by updating forcing fields, adjusting the spectral discretization and retuning wind wave growth and swell dissipation parameters. Most of the model calibration and performance analysis is done using significant wave heights (H_s) from the recent re-calibrated and denoised satellite altimeter data set provided by the European Space Agency Climate Change Initiative (ESA-CCI), with additional verification using spectral buoy data. We find that, for the year 2011, using wind fields from the recent ERA5 reanalysis provides lower scatter against satellite H_s data compared to historical ECMWF operational analyses, but still yields a low bias on wave heights that can be mitigated by re-scaling wind speeds larger than 20 m/s. Alternative blended wind products can provide more accurate forcing in some regions, but were not retained because of larger errors elsewhere. We use the shape of the probability density function of H_s around 2 m to fine tune the swell dissipation parameterization. The updated model hindcast appears to be generally more accurate than the previous version, and can be more accurate than the ERA5 H_s estimates, in particular in strong current regions and for $H_s > 7$ m.

Keywords: Wind-generated waves, WAVEWATCH III

1. Introduction

Spectral wave models are routinely used for many applications in Earth sciences and ocean engineering. Global and regional wave datasets generated through models such as WAM (WAMDI Group, 1988; Bidlot, 2005) or WAVEWATCH III®(The WAVEWATCH III ® Development Group, 2019) have helped to improve our understanding of the wind-generated wave dynamics, estimate ocean-atmosphere interactions (e.g. surface drift and air-sea fluxes), analyze extreme events occurrences, define operational conditions for shipping, offshore and port activities, and assess wave energy resources, just to name a few examples. New applications, for example in seismology (e.g. Lecocq et al., 2019) or infrasound monitoring (De Carlo et al., 2021) are made possible by the ever increasing quality of modeled wave spectra and associated parameters.

The global hindcasts presented in Part 1 (Rascle et al., 2008) and Part 2 (Rascle and Ardhuin, 2013), and the Arctic hindcast of Stopa et al. (2016b) are unique in providing wave parameters in an "Earth System" context, including wave-related fluxes of momentum and energy between the ocean, atmosphere and sea ice. These hindcasts have been used in a wide range of applications, including as a source of boundary conditions for coastal models (Roland and Ardhuin, 2014; Boudière et al., 2013), air-sea fluxes and upper ocean mixing (Wunsch and Ferrari, 2009), surface drift of kelp or plastics (Fraser et al., 2018; Onink et al., 2019; Dobler et al., 2019), and the investigation of microseisms (e.g. Nishida and Takagi, 2016; Retailleau et al., 2017). For most open ocean regions, the accuracy of significant wave height (H_s) estimates is typically better than 10%, with great benefits for the safety of life at sea, but for some regions, in enclosed seas, regions of strong currents, and near the sea ice, H_s errors typically exceed 20%, and other parameters can be much less accurate, in particular the shape of the frequency spectrum, the height of swells or the directional spreading (Stopa et al., 2016b). The reasons for these errors, and some first steps to reduce them, are the main topic of the present paper. In general the quality of numerical wave model output is a function of at least three factors, in decreasing order of importance. First, the accuracy of forcing fields (e.g. Cavaleri and Bertotti, 1997), second, the realism of parameterization of processes representing spectral wave evolution (e.g. Ardhuin et al., 2010) and third, the numerical choices made to integrate the Wave Action Equation, namely discretization and numerical schemes (e.g. Tolman, 1995; Roland and Ardhuin, 2014).

The present paper presents the effect of adjustment to model parameterizations in section 2, the impact of forcing field choices in section 3, and the influence of model discretization in section 4. We briefly discuss in section 5 alternative parameterizations that can lead to clear improvements for some parameters most sensitive to the higher frequencies of the wave spectrum but that, so far, have not led to improvements in H_s estimates and will probably require further adjustments and have thus not yet been used for the hindcast presented here. The global validation presented in section 6 shows a clear improvement on sea state parameters produced by Rascle and Ardhuin (2013) and, for specific conditions, also an improvement on the H_s estimates in the ERA5 reanalysis. Conclusions follow in section 6.

2. Model setup

2.1. Forcing fields

Because waves are forced by the wind, are damped by sea ice, and are strongly modified by currents, any improvement in the knowledge of these three forcing fields should result in better wave model results.

One of the main features in the generation of the wave hindcast analyzed in the present study, is the utilization of the wind fields from the fifth generation ECMWF atmospheric reanalyses of the global atmosphere, ERA5 (Hersbach et al., 2020), and the introduction of satellite-derived merged surface current product that combines geostrophic and Ekman currents, as produced by the Copernicus Marine Environment Monitoring System (CMEMS). The ERA5 reanalysis was developed using 4D-Var data assimilation from the Integrated Forecast System (IFS) model cycle 41r2. The number of observations assimilated from different measurement sources goes from 0.75 million per day in 1979 to approximately 24 million in 2018. The hourly output wind fields with a 31 km horizontal grid resolution, represents a clear increase in detail compared with some of its predecessors, like ERA-Interim (Dee et al., 2011). Still, the limited horizontal resolution makes the ERA5 wind fields less well resolved than those of recent ECMWF operational analyses that use a T799 Gaussian grid with an equivalent resolution of 25 km. Rivas and Stoffelen (2019) showed that ERA5 winds have a root mean square difference with the ASCAT winds that is 20% lower compared to ERA-Interim. Still, at wind speeds above 20 m/s, ERA5 biases may be as large as -5 m/s (Pineau-Guillou et al., 2018), which should have a very important impact on waves modeled with ERA5 winds.

The surface current fields were taken from the CMEMS-Globcurrent product (Global Ocean Multi Observation Product, MULTIOBS_GLO_PHY_REP_015_004), with a resolution of 3 hour in time, and 0.25 degrees in latitude and longitude. This current field is the sum of geostrophic and Ekman components based on the method of Rio et al. (2014), using an updated mean dynamic topography (MDT) from CNES-CLS (Mulet et al., 2021), which is key for the reconstruction of the ocean absolute dynamic topography from altimetry data. With the geostrophic approximation, the MDT is used to estimate surface currents.

Finally, the ice concentration is taken from the Ifremer SSMI-derived daily product (Girard-Ardhuin and Ezraty, 2012). For ice thickness, that matters most near the ice edge where it is poorly known, we have used a constant 1 m ice thickness. Partial blocking of waves by icebergs is represented following Ardhuin et al. (2011) using the Ifremer-Altiberg icebergs distribution database Tournadre et al. (2015).

2.2. Adjusted parametrizations and parameters

Atmosphere-wave interactions include both wave generation as parametrized by Janssen (1991) with modifications by Bidlot et al. (2005, 2007) and swell damping caused the air-sea friction effect decribed by Ardhuin et al. (2009). The details and adjustments of these parametrizations are described in Ardhuin et al. (2010), and Leckler (2013). Here we only recall equations where the parameters that we have tuned in the present work are included. A more comprehensive description can be found in The WAVEWATCH III® Development Group (2019).

In particular, the wind input source term was reduced by using a modified friction velocity u_* with a frequency dependent term u'_*, similar to what was done by Chen and Belcher (2000). Eqs. (20) in Ardhuin et al. (2010) is

$$S_{\rm atm}(f,\theta) = S_{\rm out}(f,\theta) + \frac{\rho_a}{\rho_w}\frac{\beta_{\rm max}}{\kappa^2 \exp(Z) Z^4 \left(\frac{u_*}{C}\right)^2} \tag{1}$$

$$\times \max\{\cos(\theta-\theta_u),0\}^p \sigma F(f,\theta) \tag{2}$$

where: $S_{\rm out}$ is the energy flux from the ocean to the atmosphere (swell dissipation term), Z= $\log(\mu)$, with μ the dimensionless critical height as given by Janssen (1991, eq. 16). $\rho_{\rm a}$ is the air density, $\rho_{\rm w}$ the water density and κ is von Kármán's constant. C is the wave phase speed, θ the wave direction, $\theta_{\rm u}$

the wind direction, and σ the wave relative frequency ($2\pi/f_r$, observed from a reference frame moving with the mean current).

In eq. (1) $\beta_{\max}$ is a non-dimensional wind-wave growth coefficient that has been used as a tuning parameter to calibrate for wind strength biases (e.g. Stopa et al., 2019). We will revisit this tuning for ERA5 winds in the present paper.

The swell dissipation parameterization is based on observations of ocean swell evolution from satellite data (Ardhuin et al., 2009). It includes expressions to take into account the effects of the transitions from (linear) viscous boundary layer to (non-linear) turbulent boundary layer. The smoothing between these two regimes accounts for the Rayleigh distribution of wave heights (Perignon et al., 2014). The negative part of the wave-atmosphere interaction, is thus parameterized as follows,

$$S_{\rm out}(k,\theta) = \quad r_{\rm vis} S_{\rm out,vis}(k,\theta) + r_{tur} S_{\rm out,tur}(k,\theta), \tag{3}$$

where the two weights give the relative importance of viscous and turbulent attenuation, and are controlled by the ratio of the significant Reynolds number $\mathrm{Re} = 2u_{\rm orb,s}H_s/\nu_a$ and its critical value $\mathrm{Re_c}$.

$$r_{\rm vis} = \quad 0.5\left[1 - \tanh\left((\mathrm{Re} - \mathrm{Re_c})/s_7\right)\right] \tag{4}$$

$$r_{\rm tur} = \quad 0.5\left[1 + \tanh\left((\mathrm{Re} - \mathrm{Re_c})/s_7\right)\right]. \tag{5}$$

Based on the analogy with oscillatory bottom boundary layers, $\mathrm{Re_c}$ was initially set to 1.5×10^5.

Wave energy loss to the ocean is dominated by wave breaking, and parameterized following the saturation-based breaking ideas of Phillips (1985). An ad hoc "cumulative term" was added to enhance the dissipation of relatively short waves (Banner and Morison, 2006; Ardhuin et al., 2010). Alternatives are discussed in section 5.

Finally, to reduce computational costs, we have used the Discrete Interaction Approximation (DIA Hasselmann and Hasselmann, 1985), to represent the 4-wave nonlinear interactions. This rather crude parameterization induces errors that are partly corrected by the other adjusted source terms in the Wave Action Equation (Banner and Young, 1994).

2.3. Spectral and spatial discretization

The wave spectrum is discretized in 24 directions, equivalent to a 15° directional resolution, and 36 exponentially spaced frequencies from 0.034 to 0.95 Hz, with a 1.1 increment factor from one frequency to the next. The selected frequency range represents a departure from our previous hindcasts (Rascle and Ardhuin, 2013), in which a narrower frequency range was employed, from 0.037 to 0.71 Hz. Although the parameterizations used here are not very accurate for frequencies above 3 times the wind sea peak (e.g. Peureux et al., 2018), the extension to higher frequencies allows to better capture the variability of the wave spectrum for very low wind speeds or very short fetches. The lower frequencies are there to let the spectrum develop for the most severe storm cases (Hanafin et al., 2012). We have used the third order Upwind Quickest advection schemes (Leonard, 1991) for both spatial and spectral advection, and the correction for the Garden Sprinkler Effect proposed by Tolman (2002).

All the model testing and tuning presented in section 2 was performed over a near-global grid with a spatial resolution of 0.5°, from 78° S to 83° N in latitude. However, all the other results, including the final hindcast, use a multi-grid system (Tolman, 2008; Chawla et al., 2013) in which regional grids provide a refinement near the coasts, the ice edge, and in regions of strong currents. A total of 7 nested grids were placed within the global grid, 6 regular grids and 1 curvilinear grid for the Arctic region. Details of the nested grids are provided in table 1 and Fig. 1. As shown in Fig. 1, the boundaries of the high resolution domains (in color) generally follow the coast at 500 km distance, including regions around Hawaii and the Tuamotus for the East Pacific grid, and the Azores for the North-East Atlantic grid. The regions in white are only covered with the global 0.5 degree resolution. The boundary conditions from a lower rank grid are taken at the edges of the colored regions in Fig. 1, and the higher rank grid results are spatially averaged to give the lower rank grid solution where these overlap (Tolman, 2008).

The benefits of the multi-grid system are particularly discussed in section 4.1. Compared to Rascle and Ardhuin (2013), including the Arctic grid allowed to provide a truly global wave hindcast.

2.4. Model tuning

The value of $\beta_{\max}$ in eq. (1), s_7 and Re_c in eqs. (4) and (5) have been adjusted to minimize the model differences against satellite altimeter mea-

Sub-Grid Name	Region	Grid type	Spatial resolution	Rank
ATNE-10M	North-East Atlantic	regular	1/6°	2
ATNW-10M	North-West Pacific	regular	1/6°	3
AFRICA-10M	Africa	regular	1/6°	3
PACE-10M	East Pacific	regular	1/6°	2
CRB-3M	Carribean Sea	regular	1/20°	3
NC-3M	New Caledonia and Vanuatu	regular	1/20°	3
ARC-12K	Arctic Ocean	curvilinear	12 km	4

Table 1: Nested grids characteristics. Global grid is defined as rank 1.

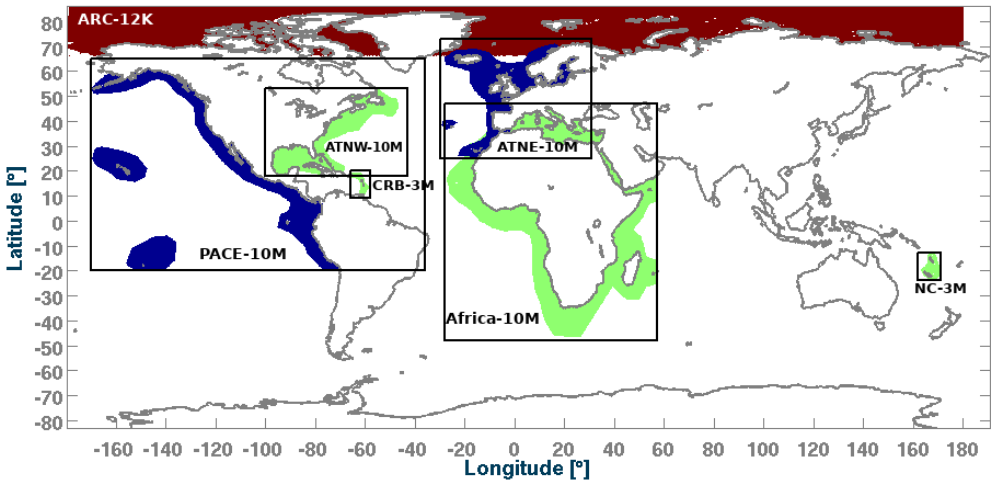

Figure 1: Sub-Grids nesting layout for multi-grid tests. Colors indicate areas where computations are performed and grids' rank in the nesting scheme: Blue is rank 2, Green is rank 3, and Red is rank 4.

surements of H_s by the Jason-2 mission for the year 2011, using the European Space Agency Climate Change Initiative data set (Dodet et al., 2020). We use a full year for calibration to properly sample all types of sea states in all seasons, and the year 2011 has been chosen because it had the highest wave heights ever recorded Hanafin et al. (2012), and this allows a sampling of the most extreme conditions. The variable used is the "denoised" significant wave height, at 1 Hz (approximately 7 km) resolution. The model tests performed and associated parameter values are listed in table 2. All test simulations are 1-year hindcasts with data output frequency of 3 hours. These tests also include some wind bias correction. This correction is defined as a

piece-wise linear correction, with modeled wind speeds above U_c multiplied by a factor x_c as follows,

$$U_{10,\mathrm{corr}} = U_{10,\mathrm{raw}} + x_c \max\left\{U_{10,\mathrm{raw}} - U_c, 0\right\}. \tag{6}$$

Name for set of parameters	$\beta_{\max}$	$\mathbf{s_7}$	$\mathbf{Re_c}$	$\mathbf{U_c}$ (m/s)	$\mathbf{x_c}$
T471f	1.33	3.60×10^5	1.50×10^5	–	–
T471	1.43	3.60×10^5	1.50×10^5	–	–
Bm1.5	1.50	3.60×10^5	1.50×10^5	–	–
Bm1.65	1.65	3.60×10^5	1.50×10^5	–	–
Bm1.7	1.70	3.60×10^5	1.50×10^5	–	–
Bm1.75	**1.75**	3.60×10^5	1.50×10^5	–	–
Bm1.65-W01	1.65	3.60×10^5	1.50×10^5	20	1.05
Bm1.65-W02	1.65	3.60×10^5	1.50×10^5	21	1.05
Bm1.65-W03	1.65	3.60×10^5	1.50×10^5	23	1.08
Bm1.65-W04	1.65	3.60×10^5	1.50×10^5	22	1.05
Bm1.7-W02	1.70	3.60×10^5	1.50×10^5	21	1.05
Bm1.7-W03	1.70	3.60×10^5	1.50×10^5	23	1.08
Bm1.7-W04	1.70	3.60×10^5	1.50×10^5	22	1.05
Bm1.75-W02	**1.75**	3.60×10^5	1.50×10^5	21	1.05
Bm1.75-W03	**1.75**	3.60×10^5	1.50×10^5	23	1.08
Bm1.75-W04	**1.75**	3.60×10^5	1.50×10^5	22	1.05
Bm1.75-W02-s7-01	**1.75**	3.96×10^5	1.50×10^5	21	1.05
Bm1.75-W02-s7-02	**1.75**	4.14×10^5	1.50×10^5	21	1.05
Bm1.75-W02-s7-03	**1.75**	$\mathbf{4.32 \times 10^5}$	1.50×10^5	21	1.05
Bm1.75-W02-s7-03-s4-01	**1.75**	$\mathbf{4.32 \times 10^5}$	1.35×10^5	21	1.05
Bm1.75-W02-s7-03-s4-02	**1.75**	$\mathbf{4.32 \times 10^5}$	1.20×10^5	21	1.05
T475	**1.75**	$\mathbf{4.32 \times 10^5}$	$\mathbf{1.15 \times 10^5}$	21	1.05

Table 2: Models parameters and their adjustments, in bold, leading to run T475. All parameters not specified here correspond to the default T471 parameterization (Rascle and Ardhuin, 2013; The WAVEWATCH III ® Development Group, 2019). Variables $\beta_{\max}$, s_7 Re_c, U_c and x_c correspond to namelist parameters BETAMAX, SWELLF7, SWELLF4, WCOR1 and WCOR2 in the WW3 input files (see Appendix A for the full set of parameters).

The normalized root mean square difference (NRMSD), scatter index (SI) and normalized mean difference (NMD) were employed to assess the model - satellite discrepancy and its change when model parameterizations, forcing or discretization are modified. These statistical parameters were calculated for the entire domain and over a set of specific ocean regions (defined in table

3), for each 1-year test in table 2. They are defined as follows,

$$\mathrm{NRMSD}(X) = \sqrt{\frac{\sum(X_{\mathrm{mod}} - X_{\mathrm{obs}})^2}{\sum X_{\mathrm{obs}}^2}} \tag{7}$$

$$\mathrm{SI}(X) = \sqrt{\frac{\sum\left[(X_{\mathrm{mod}} - \overline{X_{\mathrm{mod}}}) - (X_{\mathrm{obs}} - \overline{X_{\mathrm{obs}}})\right]^2}{\sum X_{\mathrm{obs}}^2}} \tag{8}$$

$$\mathrm{NMD}(X) = \frac{\sum(X_{\mathrm{mod}} - X_{\mathrm{obs}})}{\sum X_{\mathrm{obs}}} \tag{9}$$

where $\mathrm{X_{obs}}$ and $\mathrm{X_{mod}}$ are the altimeter significant wave heights (denoised) and the modelled H_s respectively. In particular for the tuning process, $\mathrm{X_{obs}}$ is the along-track data from the altimeter, and $\mathrm{X_{mod}}$ is obtained by interpolating the model output in space and time from the closest 4 grid points, into the position of the altimeter measurement.

We note that other normalizations could be used (Mentaschi et al., 2015), and in particular a larger scatter index is not always the indication of a poorer model performance, in particular in the presence of large biases or large fluctuations.

We particularly looked at differences for different ranges of observed values of H_s, binning all the model output as a function of the satellite values. In general, for the model's performance assessment, attention was only paid to H_s larger than 1.0 m because H_s smaller than 0.75 m is not very accurate due to limited sampling of the signal associated with the radar bandwidth (Smith and Scharroo, 2015; Ardhuin et al., 2019).

Previous parameter settings defined as "T471" were used as a starting point. After gradual increases of β_{max} without changing the other parameters (sets T471f to Bm1.75 as defined in table 2), a persistent negative NMD for H_s values larger than 7 m is found, as illustrated in Fig. 2.

This behavior is expected to be related to an underestimation of wind speeds in excess of 25 m/s in ECMWF IFS model results, including the ERA5 data set, as analyzed by Pineau-Guillou et al. (2018). This wind-speed dependent bias, which is not found with CFSR winds, was the main motivation for introducing the wind speed correction in eq. (6).

After setting $\beta_{\mathrm{max}} = 1.75$, wind speed corrections with the parameters Bm1.75-W02 helped to reduce the wave heights underestimation in the 8–14 m range (Fig. 3).

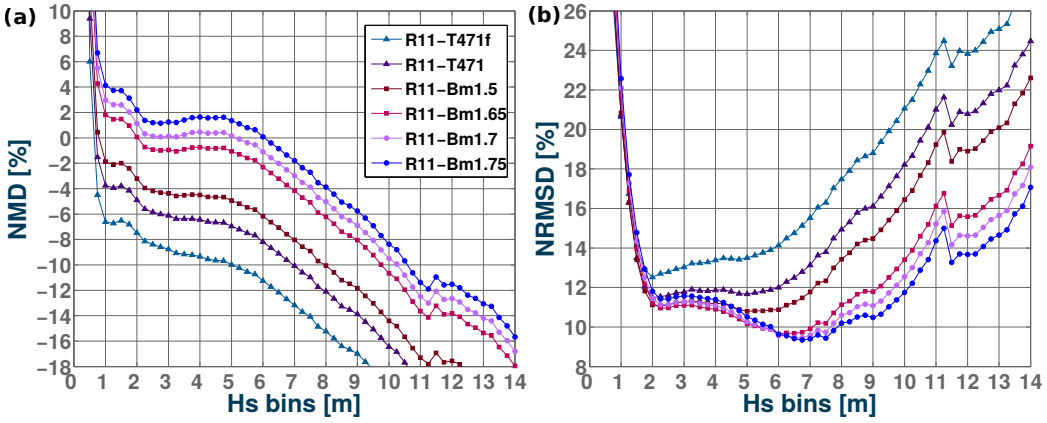

Figure 2: Error statistics for H_s for the $\beta_{\max}$ sensitivity runs (a) Normalized mean difference between model runs – with parameters given in Table 2 – and the Jason-2 altimeter data, (b) normalized root mean square difference.

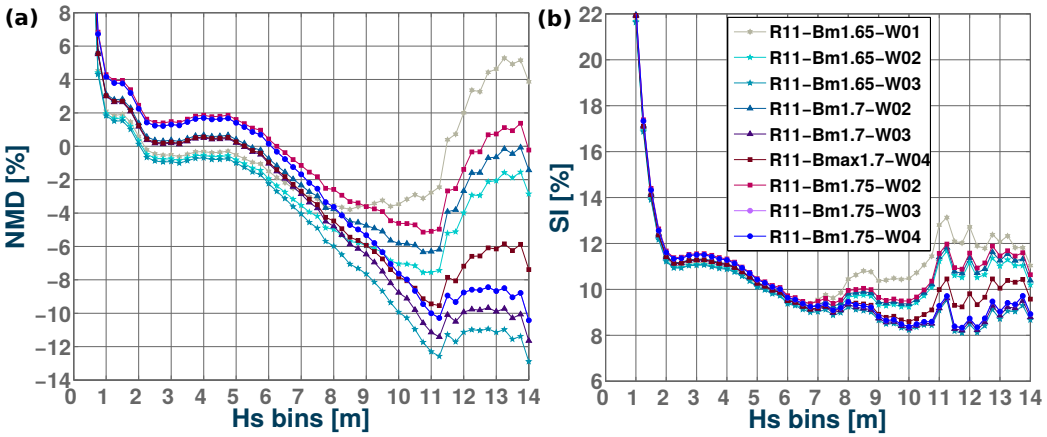

Figure 3: Error statistics for H_s for the wind correction sensitivity runs (a) Normalized mean difference between model runs – with parameters given in Table 2 – and the Jason-2 altimeter data, and (b) scatter index.

The wind speed U_c at which the correction kicks in is consistent with the analysis of models and in situ wind data by Pineau-Guillou et al. (2018), where it was demonstrated that typically strong winds above 20 m s^{-1} are underestimated by the ECMWF models.

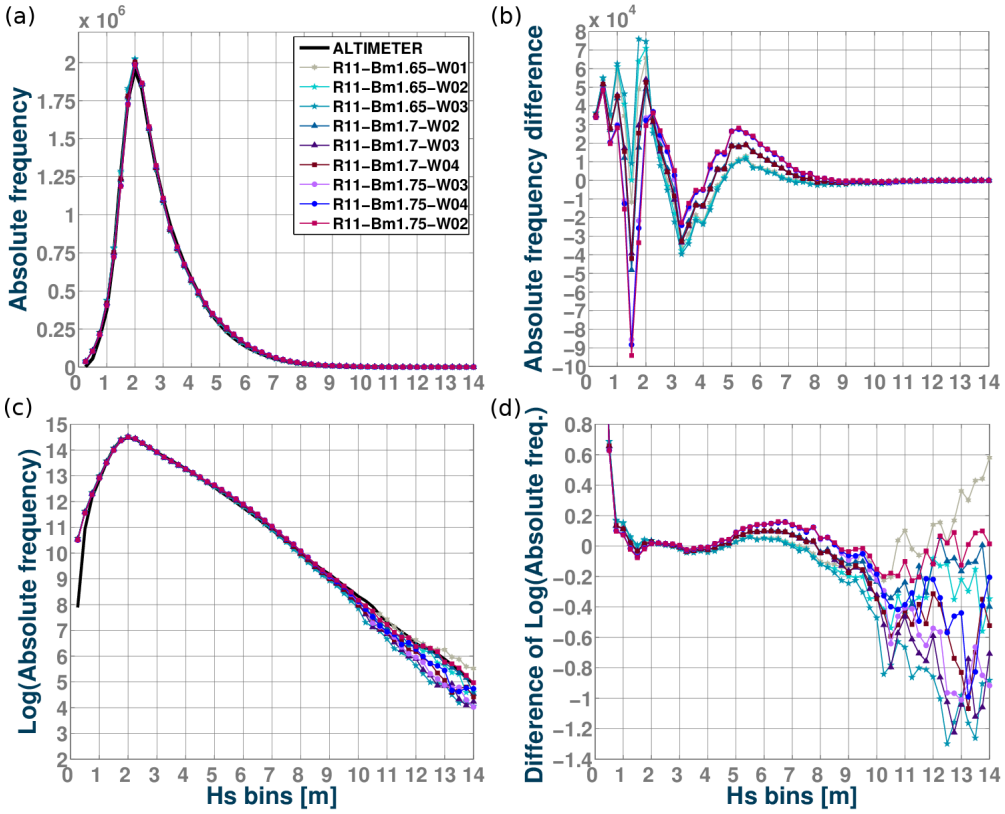

Figure 4: (a) Histogram of H_s values in the Jason-2 and co-located model simulations. (b) Differences between the model and altimeter histograms. Plots shown are from wind correction tests only. (c) Same as (a) but with a logarithmic scale. (d) Difference of logarithm of the modeled and measured H_s histograms.

Once the NMD and NRMSD were reduced, particular attention was paid to the distribution of H_s. The applied changes in $\beta_{\max}$ and wind correction lead to more intense waves in storms and swells radiated from these storms. As a result the swell dissipation necessarily needs further tuning, which is done here by adjusting s_7 and Re_c. This adjustment can be done using wave spectra measurements from buoys, but also using the distribution of H_s. Indeed, the smoothing of swell dissipation was introduced in eq. (3) by

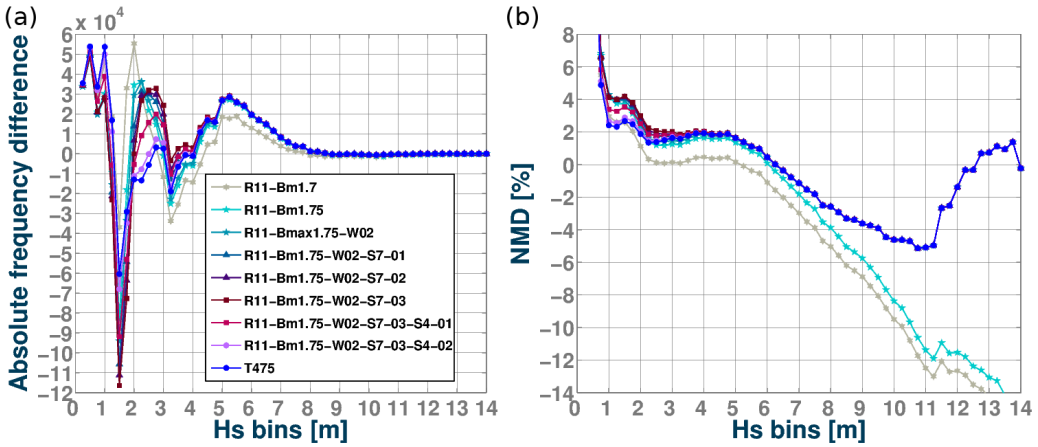

Figure 5: (a) Histogram of H_s values in the Jason-2 and model simulations absolute frequency of occurrence difference (WW3 - alitmetry data). (b) Normalized mean bias. Plots shown are from s_7 and Re_c sensitivity tests.

Leckler et al. (2013) to correct the sharp jump around 2 m in the distribution of modeled H_s that was first noted by D. Vandemark (personal communication, 2012). It was only later rationalized as an effect of the Rayleigh distribution of wave heights with turbulent boundary layers over the largest waves in a group and viscous boundary layers over the lowest waves in a group (Perignon et al., 2014; Stopa et al., 2016b). Fig. 4 shows the distribution of H_s in the model and observations. With panel b showing the difference between model and observation to make the differences more visible for wave heights smaller than 8 m, and in panel d the difference of the log of frequency of occurrence to see the deviations for larger H_s. Augmenting s_7 from 3.6×10^5 with the parameters s7-01 to 4.32×10^5 with s7-03 spreads the transition from viscous to turbulent dissipation over a wider range of H_s and tends to smooth the histogram of H_s. This corrects the bias in the distribution around $H_s = 2.0$ m but makes things worse around 1.5 m. To correct those errors requires also shifting the transition Reynolds number Re_c to lower values in runs s4-01, s4-02 and s4-03 as shown in Fig. 5.a. These later adjustments made it possible to match the occurrence of the highest values of H_s, up to 14 m, as shown in Fig. 5.b.

Although H_s gives a very limited description of the sea state, the great benefit of H_s altimeter data is their global coverage, and the differences between model and observation over different regions of the world ocean can

also be revealing due to the different types of sea states found in these regions (Chen et al., 2002), but also due to different forcing by winds, currents and sea ice. Table 3 defines the different ocean regions for which we have looked at regional H_s statistics. Further analyses on effects over the directional spreading and other wave parameters based on in-situ measurements, are presented in section 5 and 6.3 respectively.

Region (basin)	**Minimum Longitude** [°]	**Maximum Longitude** [°]	**Minimum Latitude** [°]	**Maximum Latitude** [°]
North Atlantic	-80	-5	10	50
South Atlantic	-68	20	-54	-2
North Pacific	125	-100	5	60
South Pacific	150	-73	-54	-2
Indian Ocean	50	100	-30	25
Southern Ocean	-179.98	180	-70	-55
NO SOUTH	-179.98	180	-55	66

Table 3: Regions definition for performance analysis.

The adjustments of $\beta_{\max}$ and wind intensities corrections showed particularly good improvements in the North and South Pacific. By only augmenting the $\beta_{\max}$ value (for example in tests R11-Bm1.7 and R11-Bm1.75), an important decrease of the H_s occurrences is obtained around 2 m, especially in the South Pacific, but this comes at the price of an excess of H_s values in the 1–1.5 m range (Fig. 6).

Higher values of $\beta_{\max}$ also reduced the overall negative bias in wave heights within the range of 1.5–7 m, with a further reduction of the negative NMD when the selected wind correction is applied. This specially improves the NMD for H_s of 7 to 11 m in the North Atlantic and South Pacific (Fig. 7). The South Pacific stands out as a region of high positive bias (Fig. 8).

Although it is possible that winds in the Southern Ocean may have specific biases due to a limited set of data used for assimilation, the state of the atmosphere is very much controlled by remote sensing data, including radiometers and scatterometers that are assimilated globally (Hersbach et al., 2020).

Another peculiarity of the Southern Ocean is the importance of the circumpolar current that generally flows from West to East. Not taking it into account is known to produce a large positive bias of the order of 20 cm

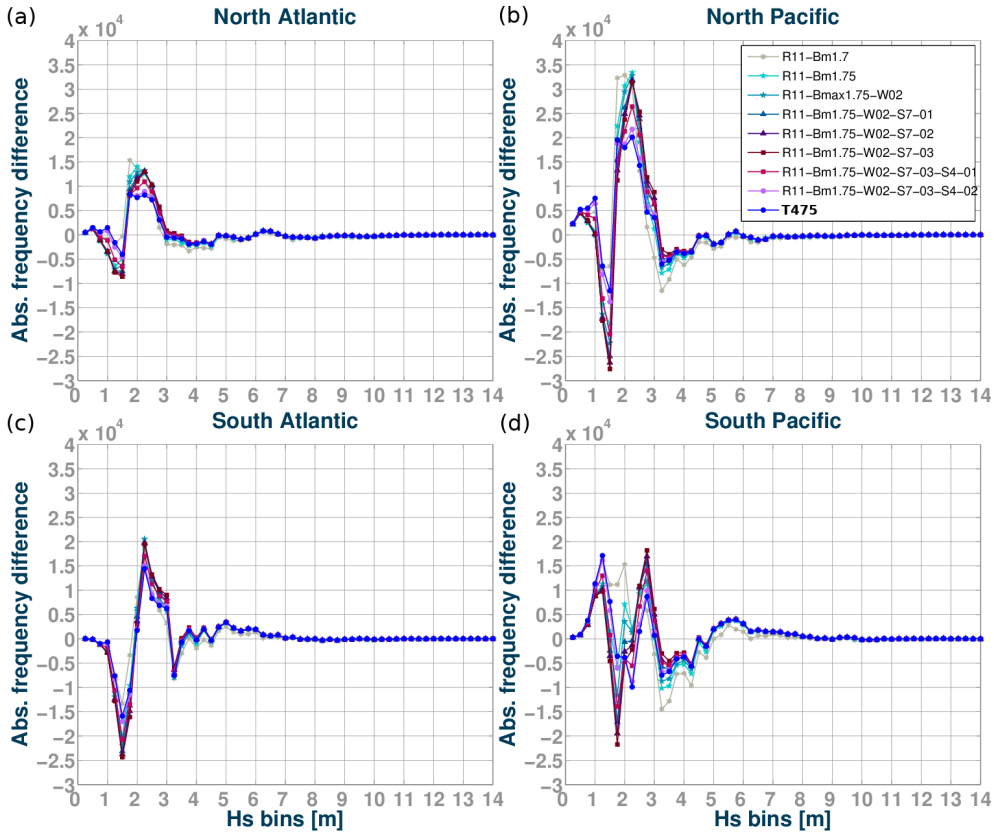

Figure 6: H_s absolute frequency of occurrence difference (WW3 - altimetry data) from Atlantic and Pacific basins.

in wave heights due to the relative wind effect (Rascle et al., 2008; Rapizo et al., 2018), and large gradients in H_s associated to refraction (Quilfen and Chapron, 2019). Indeed, the relevant wind speed for wave generation is the wind velocity minus the surface current velocity. However, these previous estimates use numerical models that are not very reliable for surface current estimates (ESA, 2019). Another effect specific to the Southern Ocean is the presence of both sea ice and icebergs, with a very large impact on wave heights (Ardhuin et al., 2011). The year 2011 has a rather large anomaly in iceberg numbers, although not as large as in 2009 (Tournadre et al., 2016). Finally, the details in sea ice concentration near the ice edge and the parameterizations of wave-ice interactions are another important source of uncertainties at latitudes south of 55°S (Doble and Bidlot, 2013; Ardhuin et al., 2020).

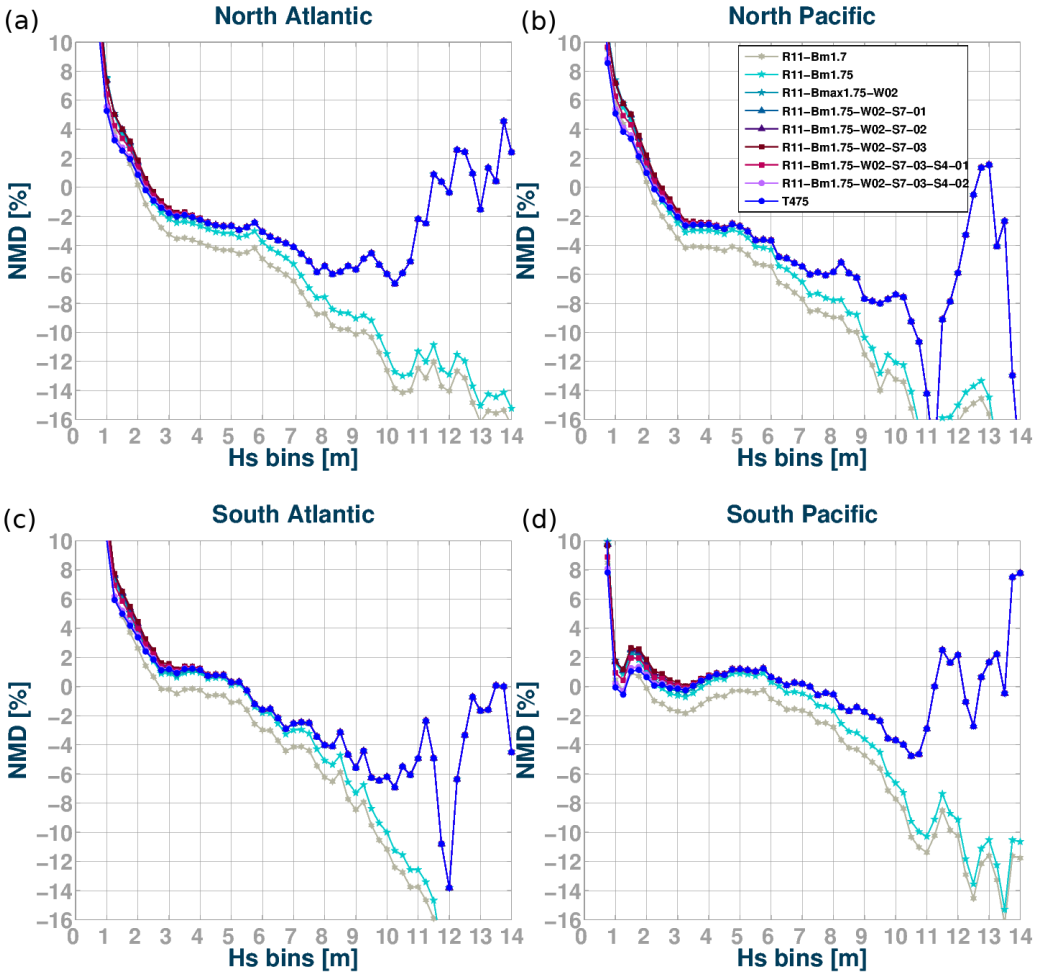

Figure 7: H_s NMD within Atlantic and Pacific basins as a function of observed wave heights. H_s bins' range is 0.25 m.

For these reasons, we now investigate alternative forcing fields for winds, ice and currents, and their impact on the model results.

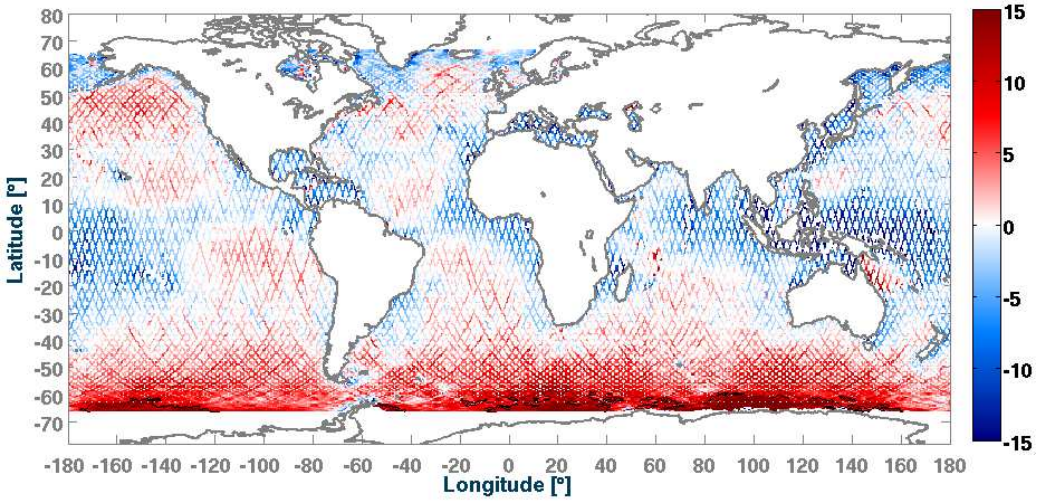

Figure 8: NMB for 1-year averaged H_s using ERA5 winds. Modelled year: 2011. Parameter settings from test T475. Colorbar indicates NMD values in %. Black lines represent positive 10 % contours.

3. Influence of forcing field choices

As we did for the choice of model parameters, forcing set-up and model adjustment was done over the year 2011, with a complete validation on other years described in section 6. Whereas we had used Jason-2 data only for the model calibration, we now use the full ESA Sea State Climate Change Initiative merged altimeter data set, using the denoised 1-Hz data for the significant wave height (Dodet et al., 2020). For the year 2011 this includes data from the following satellite missions: Jason-1, Envisat, Jason-2 and Cryosat-2. Using the model with parameters T475, our baseline model run uses ERA5 winds, Ifremer sea ice and iceberg concentrations, and CMES-Globcurrent surface currents.

3.1. Choice of forcing wind field

We now look at three alternative wind fields. These include the operational ECMWF IFS winds which, for the year 2011, was obtained with IFS cycle 37r2, an earlier and less accurate version of IFS compared to the 41r2 used for ERA5. We also considered the CFSR winds (Saha et al., 2010) that were used by Rascle and Ardhuin (2013). Finally we tested the Ifremer CERSAT Global Blended Mean Wind Fields (Bentamy et al., 2018), from here on just named "Ifremer". Other wind fileds like ERA-Interim and MERRA2

(Gelaro et al., 2017) have also been considered in other hindcasts such as Sharmar et al. (2021), with analyses focused on inconsistencies and trends of the different atmospheric forcing.

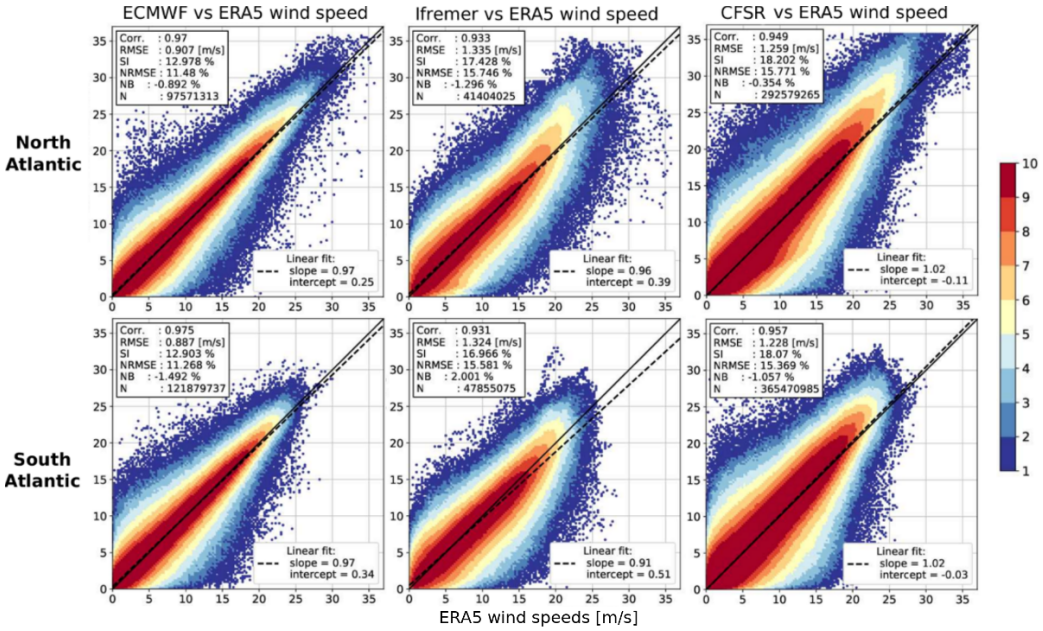

Figure 9: Scatter plot of wind speed for the months of January to July 2011. ERA5 intensity bins along x-axis. Top panels: ECMWF operational product vs ERA5, Middle panels: Ifremer vs ERA5. Bottom panels: CFSR vs ERA5. Colors give the logarithm of the number of data points in each 0.25 m/s×0.25 m/s wind speed bin.

The main difference between the Ifremer winds and the 2 other data sets, is that the Ifremer 6-hourly surface wind fields are estimated mainly from scatterometer wind vector observations, merged with wind magnitude measurements from radiometer data (SSM/I, SSMIS, WindSat) and the ERA-Interim atmospheric wind reanalyzes. Further details on the product and methods can be found in Bentamy et al. (2012, 2013).

As discussed by Rascle and Ardhuin (2013) and Stopa et al. (2019), different wind fields are biased relative to one another. This is true for the average values around 7 m/s, and biases are even larger for high speeds over 20 m/s (Pineau-Guillou et al., 2018). This is shown again here in Fig. 9. The NCEP operational GFS model (not shown here) and CFSR hindcast both have wind speeds higher than those produced by the ECMWF models (operational IFS results and ERA5 results), leading to higher wave heights

when using NCEP winds. Because the Ifremer blended wind product uses ERA-Interim as a background "filler" when and where observations are too far in space or time, these data sets where homogenized to have the same low bias for average conditions (slope of 0.91 for the Ifremer wind vs the ERA5 winds in the South Atlantic) but higher values for wind speeds above 20 m/s that are more frequent in the North Atlantic.

There is also a clear indication that ECMWF operational winds give higher values for wind speeds above 20 m/s compared to ERA5, probably due to the higher resolution of the operational IFS model (25 km approx. and hourly output for 2011). The consequences of these wind field properties on the wave height biases are shown in Fig. 10.

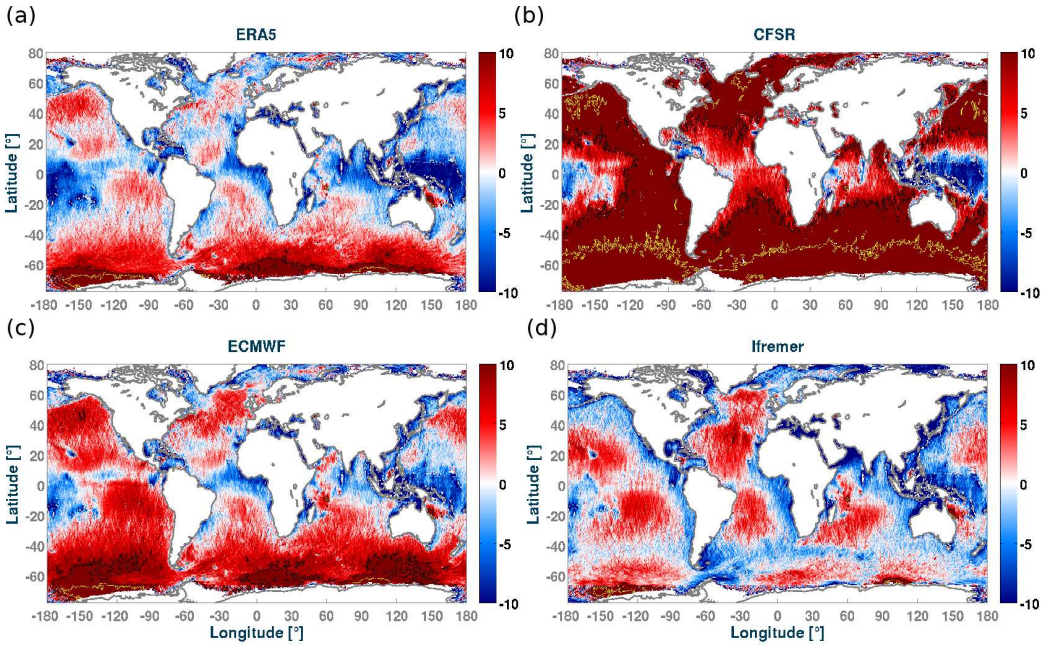

Figure 10: Normalized Mean Difference of modelled H_s minus Sea State CCI Altimeter data, averaged over the year 2011, using (a) ERA5, (b) CFSR, (c) ECMWF operational deterministic products and (d) Ifremer winds. The model was run with the set of parameters T475 as given in Table 2. Colorbar indicates NMD in percent. Black and yelow lines mark the +10 and +20 % contours.

Given the relative biases of the different wind datasets, it is not surprising that, without any retuning, the T475 set of parameters gives large H_s biases when used with other wind forcing than ERA-5. In particular the CFSR

winds give positive biases larger than 15% over most of the oceans.

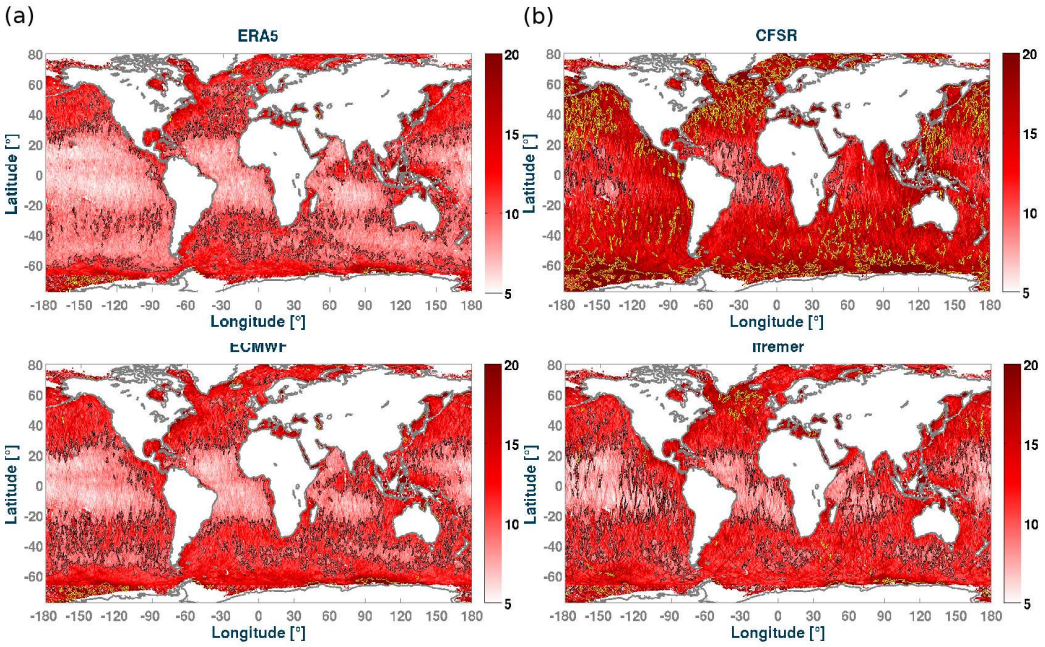

Figure 11: Scatter Index of modelled H_s minus Sea State CCI Altimeter data, averaged over the year 2011, using (a) ERA5, (b) CFSR, (c) ECMWF operational deterministic products and (d) Ifremer winds. The model was run with the set of parameters T475 as given in Table 2. Colorbar indicates SI in percent. Black and yelow lines mark the +10 and +20 % contours.

The Ifremer winds have interesting properties and are probably more realistic in some regions, where they give lower scatter index (Fig 11.d), including the southern ocean where the bias is also lower and significantly different (Fig. 10.d). This difference between Ifremer and ERA5 winds is possibly due to the fact that the remote sensing data used in the Ifremer product generally measures a wind that is relative to the current and not an absolute wind (Quilfen et al., 2004). There is also probably a contribution to the generally low bias of the ERA-Iterim product that is used to fill in between the different satellite passes.

3.2. Effects of wave-ice parametrizations and forcing fields

Much work has been done on the interactions of waves and sea ice in the recent years, with a large emphasis on pancake ice (Thomson et al., 2018),

that is particularly relevant near the ice edge and during the freeze-up period (Doble et al., 2003). Here we have rather used a parameterization associated to the presence of larger floes and their possible break-up induced by waves. In particular the formulation we have used in our baseline simulation was developed by Boutin et al. (2018) and adjusted by Ardhuin et al. (2020) to 2 months of waves measured in the sea ice of the Ross sea. That parameterization combines both wave scattering in sea ice with a wave-induced ice break-up (IS2) and dissipation below ice plates including a smooth laminar to rough turbulent flow as a function of the boundary layer Reynolds number (IC2, Stopa et al., 2016b). Given uncertainties on ice thickness, in particular in the Southern Ocean (Williams et al., 2014) and around the ice edge where it matters for wave-ice interactions, we have chosen a crude and simple constant thickness of 1 m. This parameterization is compared to the old default WW3 parameterization that is a 40 km exponential decay of wave energy proportional to the ice concentration (IC0 parameterization). The new IC2+IS2 parameterization gives a much weaker attenuation near the ice edge, and thus a larger value of H_s in the open ocean where we have data for validation (Fig. 12a,b). We have not attempted to validate the predicted wave parameter and maximum floe size in the ice-covered regions. We note that the scatter index is generally reduced around the ice, especially around Greenland and in the Ross sea. These areas typically require more validation, and the model resolution (0.5°) is probably marginal for the Southern Ocean, whereas the 12 km resolution in the Arctic allows a more detailed investigation of wave-ice interactions.

Much less work has been devoted to the effect of icebergs, so we use here the parameterization proposed by Ardhuin et al. (2011). We verify that including icebergs has a very positive effect on reducing the bias and scatter index where the icebergs are present. For the year 2011, a large concentration of icebergs was found in both the South-East of the Pacific and the South of the Indian ocean, giving a bias reduction up to 10 percentage points and, locally, a very large reduction in scatter index up to 6 percentage points (Fig. 12c,d). The concentration of icebergs in the South Pacific in 2011 is associated with two large icebergs, C19a and B15j, that drifted northward and eastward within the Antarctic Circumpolar Current (Tournadre et al., 2015, 2016), later breaking up into hundreds of smaller icebergs. These small icebergs are much more effective in reducing the wave energy flux, compared to a single parent iceberg, as they have a much larger cross section.

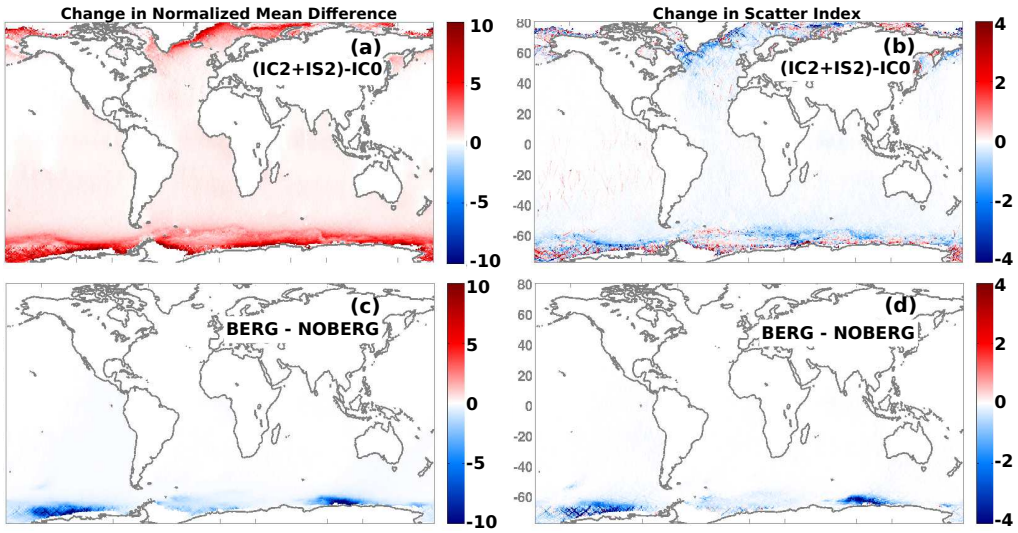

Figure 12: (a,b) using dissipation, scattering and ice break-up (IC2, IS2) or partial ice blocking (IC0) Differences in NMB and SI in percentage points for the T475 parameterization variations when using: (c,d) iceberg forcing or no iceberg forcing.

3.3. Effect of currents

Ocean surface currents can have large influences on the wave field either locally through the relative wind effect and advection, or down-wave of current gradients, due to refraction, with larger effects associated to larger current magnitude (Ardhuin et al., 2012). An important difficulty for properly taking currents into account at global scales is that there are no global observations of the Total Surface Current Velocity (TSCV) that matters for wind waves, and the only proper surface measurements are made with High Frequency radar near the coasts (Barrick et al., 1974; Roarty et al., 2019). Instead, the closest global proxy is given by the drift velocity around 15 m depth provided by instruments of the Surface Velocity Program (Elipot et al., 2016; Lumpkin et al., 2017), with only about 1500 drifters globally giving a 500 km resolution. We note that at the Equator and a few other places of interest, the 15-m depth drift is often in the opposite direction of the surface drift. Most importantly, finer spatial resolution is needed, typically down to 30 km, to represent most of the refraction effects (Ardhuin et al., 2017a; Marechal and Ardhuin, 2020). As a result, surface current estimates are often taken from numerical models, or, which is the case of the CMEMS Globcurrent product used here, derived from combined obser-

vations of sea surface height anomaly, mean dynamic topography and surface winds, assuming a quasi-geostrophic equilibrium of the Coriolis force associated to the surface current with the combination of the wind stress and the pressure gradient associated to sea surface height. Except possibly for western boundary currents such as the Gulf Stream or the Agulhas, this approach does not work very well, in particular around the equator and in mid-latitudes where currents are dominated by near-inertial currents as illustrated in Fig. 13. The CMEMS Global Ocean Multi Observation Products (MUL-

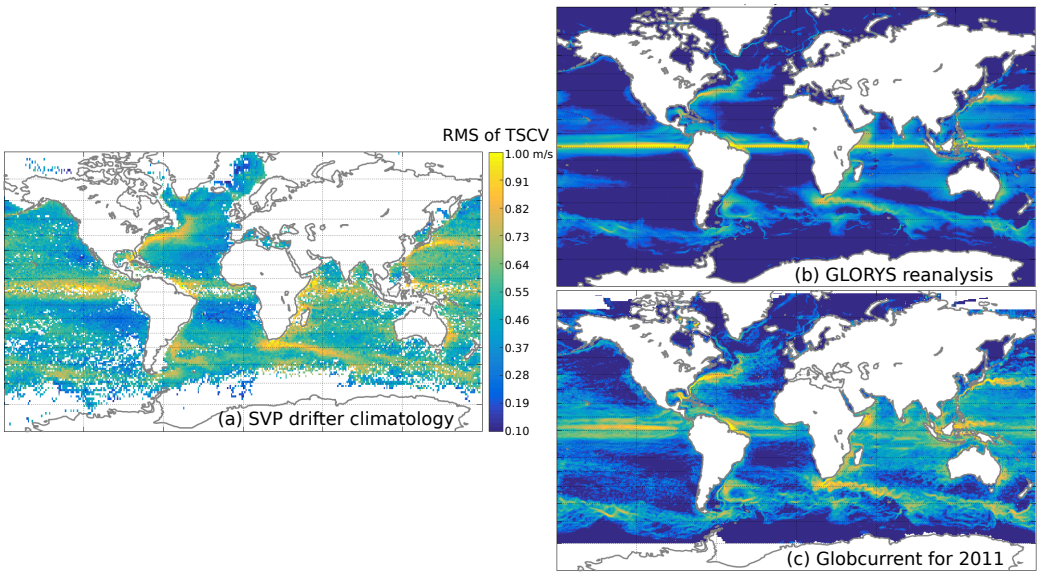

Figure 13: Root mean square current velocity (a) at 15 m depth using in situ drifter data from the Surface Velocity Program (SVP) processed by Elipot et al. (2016) with rms velocity computed over 30-day long trajectories and attributed to the center of that trajectory and white ocean pixels corresponding to 1 by 1 degree squares in which no data was available, (b) as given by the CMEMS GLORYS reanalysis, (c) as given by the CMEMS-Globcurrent product based on altimeter sea level anomalies, mean dynamic topography inferred from satellite gravimeters and ocean drifters, and "Ekman currents" estimated from ECMWF wind analyses.

TIOBS_GLO_PHY_REP_015_004) has an average current that is closer to the SVP drifter climatology than the CMEMS Global Ocean Reanalysis (GLORYS) product GLOBAL-REANALYSIS-PHY-001-031, in particular around the Equator, which is why we have chosen to use the former product as our TSCV forcing.

Given all these limitations it is not specially surprising that the TSCV is

seldom used at global scale. Including the TSCV forcing can indeed increase errors in some regions due to errors in the forcing field, but it generally corrects part of the bias and gives lower scatter index for wave heights compared to altimeter data, as illustrated in Fig. 14. Comparing our simulation with parameters T475 with and without currents, we find a clear lower bias along the Equator and in the Southern ocean when currents are used, as already reported by Rascle et al. (2008). This is probably associated with the relative wind effect, with wave generation given by the difference between the wind vector and the TSCV and not the wind vector alone. We know that this approach can overestimate the current effect when the atmosphere model is not coupled with an ocean model (Hersbach and Bidlot, 2008; Renault et al., 2016), however, we also expect that the TSCV is generally underestimated by the CMEMS-Globcurrent product.

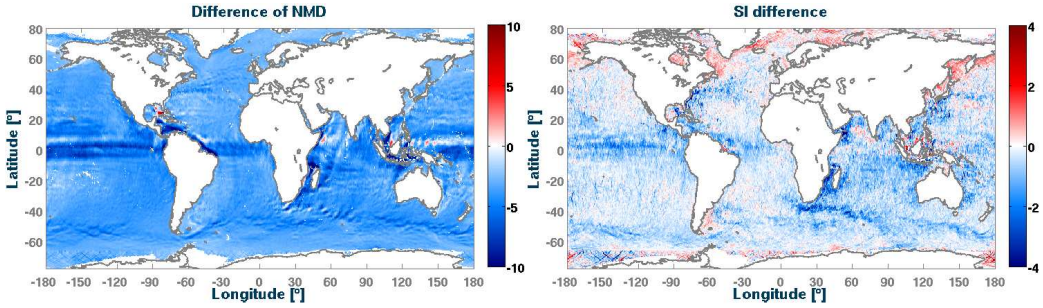

Figure 14: Left: Change in Normalized Mean Difference (NMD in percentage points) for H_s with currents and the T475 parameterization versus the same simulation without current. For both simulatons the reference is the Sea State CCI H_s for the year 2011. Right: same for difference in SI, with the dark blue corresponding to a reduction of 4 percentage points (e.g. from 14% to 10%) when TSCV forcing is used.

The reduction of the scatter index against altimeter H_s that is brought by the current (blue regions in Fig. 14.b) clearly corresponds to the regions of strong currents where the variability of incoming waves can cause a large variability of the wave heights around the current: this is the case in the Agulhas current, in the Gulf Stream, the Kuroshio, the Mozambique channel, the Somali current. However, as shown in Fig. 11, these regions are still places where the models error are relatively large, possibly due to a combination of factors, including errors in the TSCV fields, insufficient directional resolution of our wave model (Marechal and Ardhuin, 2020), and insufficient spatial resolution in the TSCV field and/or the wave model. We note that

the scatter index is generally increased for latitudes above 50° N, probably due to an insufficient resolution of the altimetry where the Rossby radius of deformation is less than 50 km (Ballarotta et al., 2019). Given the importance of the spectral and spatial discretizations, we now discuss theses aspects.

4. Model discretization

The choice of spatial and spectral discretizations can have a large impact on the model solutions, and it also has a direct and clear impact on the cost of the model, the time needed to perform the simulations. As a result, the particular choices we made for the discretizations are a compromise between the computational cost and the accuracy benefits. The 28-years hindcast used around 500,000 cpu hours distributed over 504 processors, distributed in 18 nodes that each hold 28 CPUs and 75Gb of memory.

4.1. Spatial resolution

Using higher resolution grids is critical for resolving smaller scale variations in the sea state that are caused by the time-varying forcing fields (wind, current, sea ice) or fixed features (shoreline, water depth, bottom sediment type and grain size). In practice, small scale gradients in wave heights are dominated by the distance to the coast and the presence of strong currents (Quilfen and Chapron, 2019). Because some important current system are located close to coasts, we have chosen to define nested grids that cover the relatively shallow waters of the coastal regions and, where possible, extend over strong current regions (Fig. 1). As a result, our North-West Atlantic grid covers the Grand Banks and the Gulf Stream, as well as the entire gulf of Mexico. In a similar fashion, the Africa grid was extended to the south to cover the Agulhas current retroflexion. Using different grids also allows to tune the model parameters locally.

Because the wind-wave growth tuning that corresponds to T475 is very similar to T471, it tends to give an underestimation of the wave height for short fetches (Stopa et al., 2016a). This effect is more pronounced with higher resolution grids, which explains the general reduction in wave height for enclosed seas and eastern coasts (stronger negative bias, in blue in Fig. 15.a). We also find that the explicit higher resolution of shorelines and islands gives larger H_s values compared to the subgrid treatment of complex shorelines and islands in a coarser grid (Chawla and Tolman, 2008), explaining the more

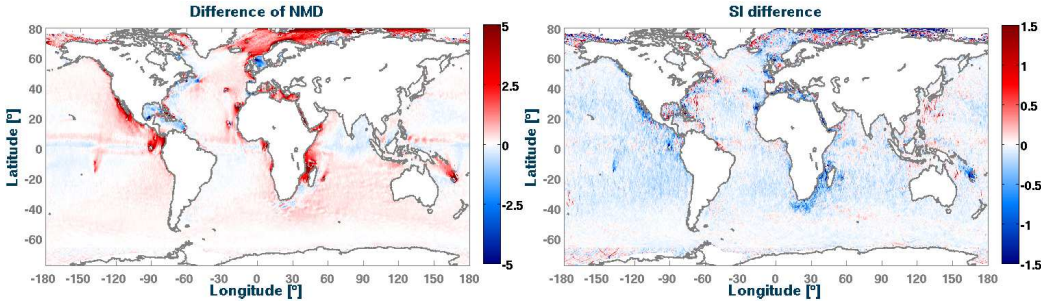

Figure 15: NMD and SI variations in percentage points for the year 2011: values for Multi-grid minus values for Single grid setup, both using the same T475 parameters. Left panel: Difference in NMD values, in this case red values represent a reduction of the negative NMD.

positive bias around 140E 10S, downwave of the Tuamotus, or around the Galapagos, Azores etc. The presence of the full Arctic ocean thanks to the Arctic grid also adds wave energy that was otherwise missing in the near-global grid that stopped at 83°N.

Overall, the scatter index is reduced over most of the ocean with the strongest reduction in regions of strong currents like the Agulhas current, or along complex coastlines such as the Baja California peninsula (blue regions in Fig. 15.b).

4.2. Spectral grid and resolution

However, to converge to the true solution of the wave action equation, increasing only the spatial resolution is not enough, and a finer spectral resolution is also needed, in particular for parameters sensitive to numerical diffusion like the directional spread (Ardhuin and Herbers, 2005). Although we know that current effects on wave heights would be better resolved with 48 directions instead of only 24 (Ardhuin et al., 2017b; Marechal and Ardhuin, 2020), we have stuck to 24 directions only because of the much lower CPU cost, and because differences in wave heights when using 24 or 36 directions were fairly limited. Fig. 16.b shows a change in the Normalized Mean Difference that is mostly limited to the tropical regions, especially around coasts and islands for which the finer directional resolution must have an impact on swell propagation, but the change in scatter index is typically much less than 1 percentage point (Fig. 16.d).

Compared to the costly increase of directional resolution, we found a higher benefit in terms of H_s accuracy in increasing the spectral range with

a maximum frequency of 0.95 Hz instead of the 0.72 Hz used by Rascle and Ardhuin (2013). This higher frequency gives a better response, in particular for the short fetch and low wind conditions in which the peak of the wind sea would otherwise not be well resolved.

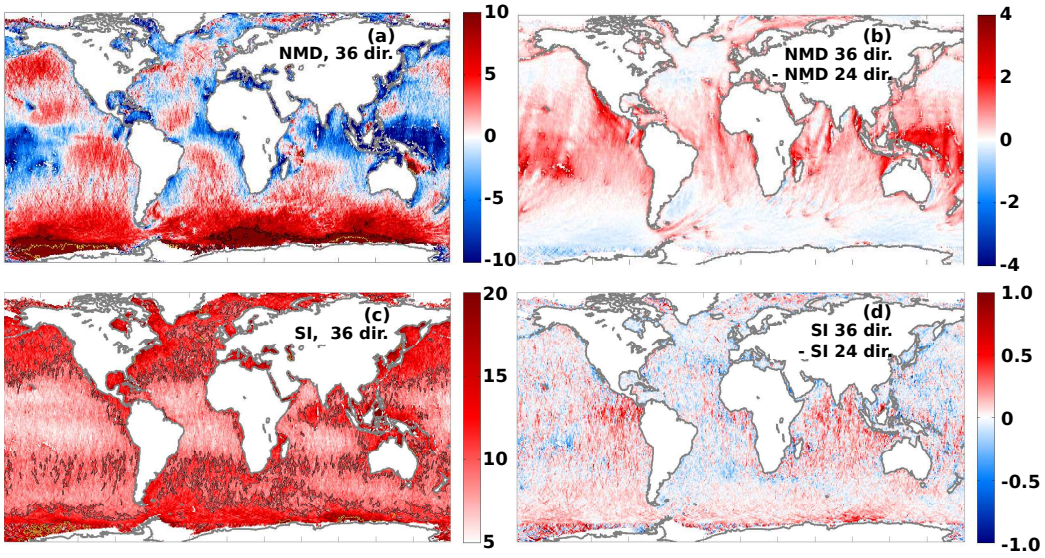

Figure 16: (a)NMD for 1 year averaged H_s using T475 with 36 directions and (b) differences in NMD for T475 with 36 directions with respect to 24 directions (Fig. 10a). Black lines mark the positive 10 % contours. (c) SI for 1 year averaged H_s using T475 with 36 directions and (d) SI difference for T475 with 36 directions with respect to 24 directions. Analyzed year: 2011. Black and yellow lines mark the positive 10 and 20 % contours respectively

5. Wave directionality and alternative dissipation parameterizations

As noted by Stopa et al. (2016b), the directional spread (Kuik et al., 1988) is the least well predicted parameter among the most common metrics used to define the shape of the wave spectrum. Whereas the mean direction is well controlled by the wind evolution and the time scale of adjustment of the wave field, the directional spread is probably influenced by details of the wave generation and dissipation parameterizations. Here we use 3-hour averaged data from WMO buoy 46436 in the North East Pacific as an example (see table 4 and Fig. 17), which is the station 166 of the Coastal

Data Information Program and is maintained by Thomson et al. (2013). The correlation coefficient for $\sigma_\theta(f)$ falls below 0.7 for frequency above 0.3 Hz. Indeed, the model has no skill in predicting $\sigma_\theta(f)$ for $f > 0.5$ Hz, and the shape of the modeled spectral tail is given by the shape at frequency f_m with an energy level decreasing like $(f_m/f)^5$, where f_m is a dynamically adjusted maximum prognostic frequency, set to 2.5 times the mean frequency of the wind sea part of the spectrum.

We note that the directional spread at low frequencies is, close to coasts, very sensitive to shoreline reflections (Ardhuin and Roland, 2012). Whereas this has a limited impact on most wave parameters, it is a critical contribution to microseism and microbarom sources (Stutzmann et al., 2012; De Carlo et al., 2021). In the present hindcast we have not used the slope-based reflection coefficient proposed by Ardhuin and Roland (2012) because of the difficulty of defining the proper slope and mixed results when validating modeled microseisms. Instead, we have used constant reflexion coefficients of 5%, 10% and 20% for the resolved shorelines, subgrid shorelines and icebergs, respectively. Clearly that parameterization will have to be tested and futher improved upon using buoy directional spreads together with microseism and microbarom data.

The T475 parameterization is thus still fairly poor for the frequency range 0.4 to 1 Hz when the waves are developed (when the wind sea peak frequency is below 0.15 Hz), in particular for the directional distribution (Fig. 17.d), which is critical for the ratio of crosswind to downwind mean square slope (Munk, 2009), wave breaking statistics (Romero et al., 2017) and the sources of microseisms and microbaroms at seismic or acoustic frequencies above 0.8 Hz (Farrell and Munk, 2010; Peureux and Ardhuin, 2016; De Carlo et al., 2020). Recent work have suggested that the shape of the dissipation function could be better described by Romero (2019), giving the T700 set of parameters in the WAVEWATCH III model, available in versions 7.0 and above. In T700, the ad hoc and not very effective cumulative term of Ardhuin et al. (2010) is replaced with a cumulative term that could be explained by the straining of short waves caused by long waves (Peureux et al., 2020). Preliminary tests reveal an interesting behavior for the shape of the high frequency spectrum (Fig. 18), which allows to remove the imposed diagnostic tail for $f > f_m$ thanks to a completely local (in the spectral sense) parameterization of the breaking probability, and the added cosine-squared angular dependence in the parameterization of the cumulative effect. Possibly this imposed shape of the cumulative term will have to be revised, as for example

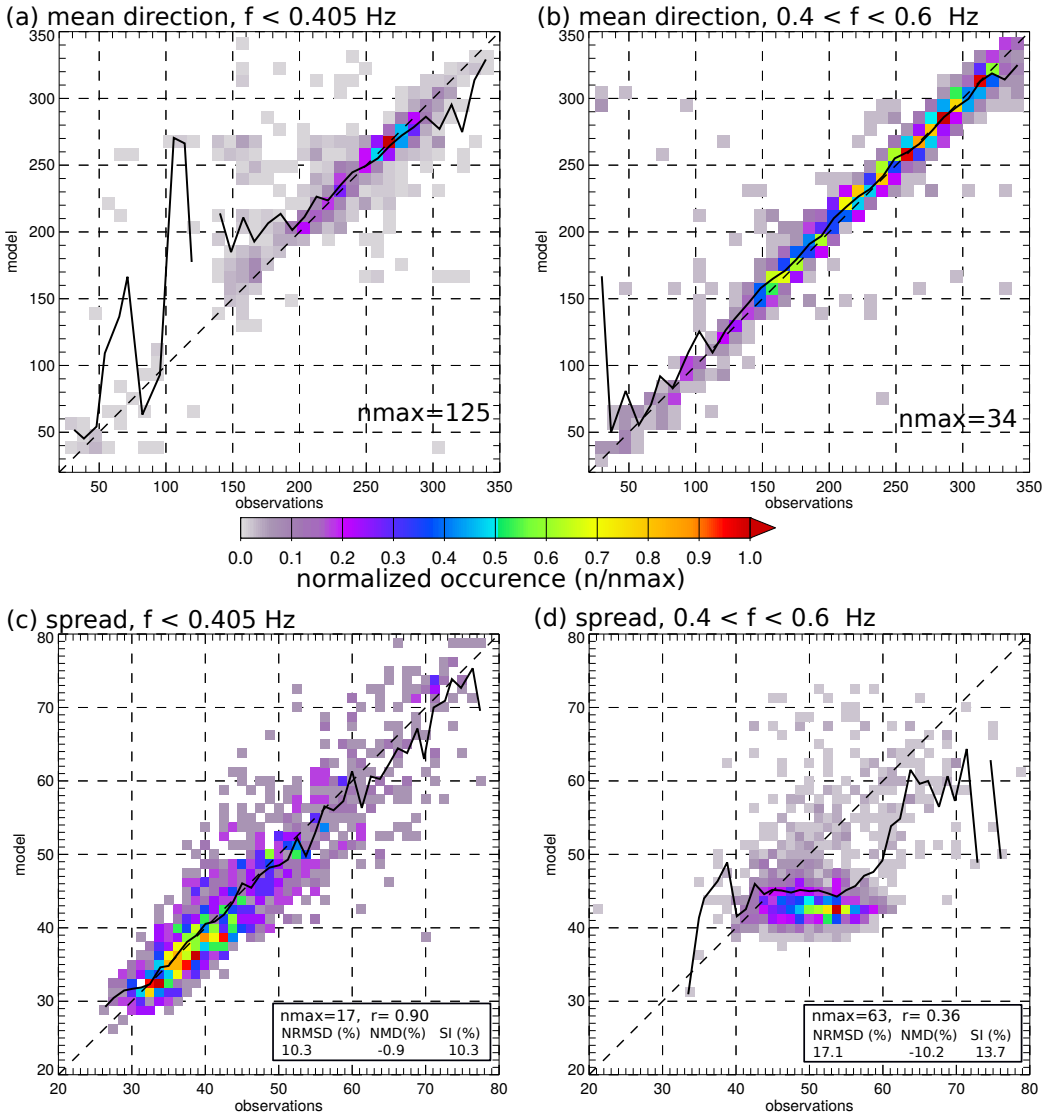

Figure 17: Modeled spread and mean direction for low frequencies ($f < 0.4$ Hz) and high frequencies ($f > 0.4$ Hz) at buoy 46246 for the year 2018. Colors show the number of 3 hour records for which the model-buoy pair falls in one bin, as normalized by the maximum value nmax. The solid lines gives the mean modeled value for each observation bin.

an isotropic spectrum of long waves should produce an isotropic effect unless it is a joint effect of the long and short waves. However, Romero (2019) has produced the first parameterization that is able to produce larger cross-wind

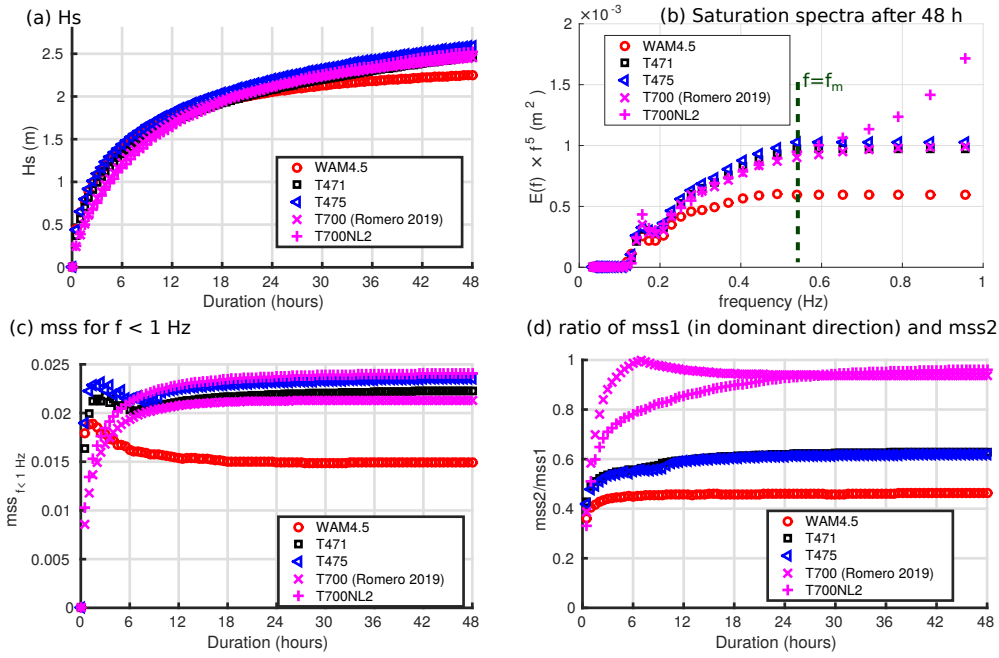

Figure 18: Differences in model results for an academic case considering a uniform ocean and a constant wind speed of 10 m/s starting from no waves. The WAM4.5 parameterization is close to the one used in the ERA5 reanalysis, and the T700NL2 corresponds to the parameterization of Romero (2019) with the non-linear interactions computed with the exact Webb-Resio-Tracy method van Vledder (2006).

slopes than down-wind slopes for wavelengths around 1 m (after 7 hours in Fig. 18.d, the dominant direction for mss1 in T700NL2 is indeed the cross-wind direction), which are critical to explain the first of the inconvenient sea truths highlighted by Munk (2009).

Taken "out of the box" without the present retuning, the Romero (2019) parameterization performs similarly to T471 in terms of scatter index but has a 2 to 6% higher value of wave height (Fig. 19) that will also require an adjustment of the swell dissipation. The benefits of such a parameterization will probably be most important for the model parameters that are most sensitive to the high frequencies, including the mean square slope, and will require an important upgrade of the wave model in the way these shorter wave components are treated, so that the wave model result can be validated with radar back-scatter data (e.g. Nouguier et al., 2016). This effort is beyond the scope of the present paper and will be discussed in Part 4.

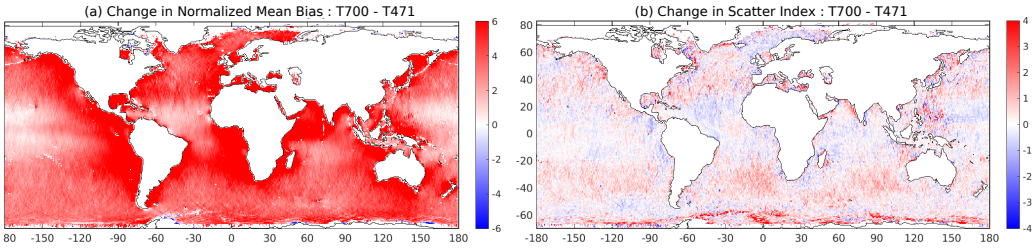

Figure 19: Change in NB and SI from the T471 to T700 change in parameterization for the year 2018. These simulations did not include ocean currents.

6. Validation

6.1. Validation with altimeter data

An important concern about numerical wave model hindcasts for all applications is their consistency in time which can be compromised by the time-evolving error statistics of the forcing fields (winds, currents, sea ice) and/or of the assimilated data which may both introduce time varying biases and jumps, possibly requiring the statistical adjustment of the forcing fields (e.g. Stopa et al., 2019) or the correction of the model results. It is thus necessary to verify the consistency of the model output over time. This requires validation data that are stable in time. Here we use the satellite altimeter H_s measurements of Dodet et al. (2020) that were especially designed for this purpose, and we look at the evolution of the NMB and SI over the years 1997 to 2018 (Fig. 20). We find a general agreement over the years, with lower variations of the mean difference than was found by Rascle and Ardhuin (2013) when using CFSR winds, and which had to be corrected in later hindcasts (Stopa et al., 2019). Still, the changes from -1 to 2% for the bulk of the data ($1.5 < H_s < 4$ m) suggest a systematic drift in either the ERA5 wind speeds or the altimeter data, with relatively flatter biases as a function of H_s for the years 2011-2018 (but still a decrease in the mean model values or an increase in the altimeter values), and steeper H_s-dependent biases for the years 1997-2010. The scatter index shows a general reduction of the random differences that can be caused by a reduction in the random noise of satellite altimeter data for the more recent missions and an improvement in the quality of the ERA5 wind fields thanks to the assimilation of a richer set of data (Hersbach et al., 2020).

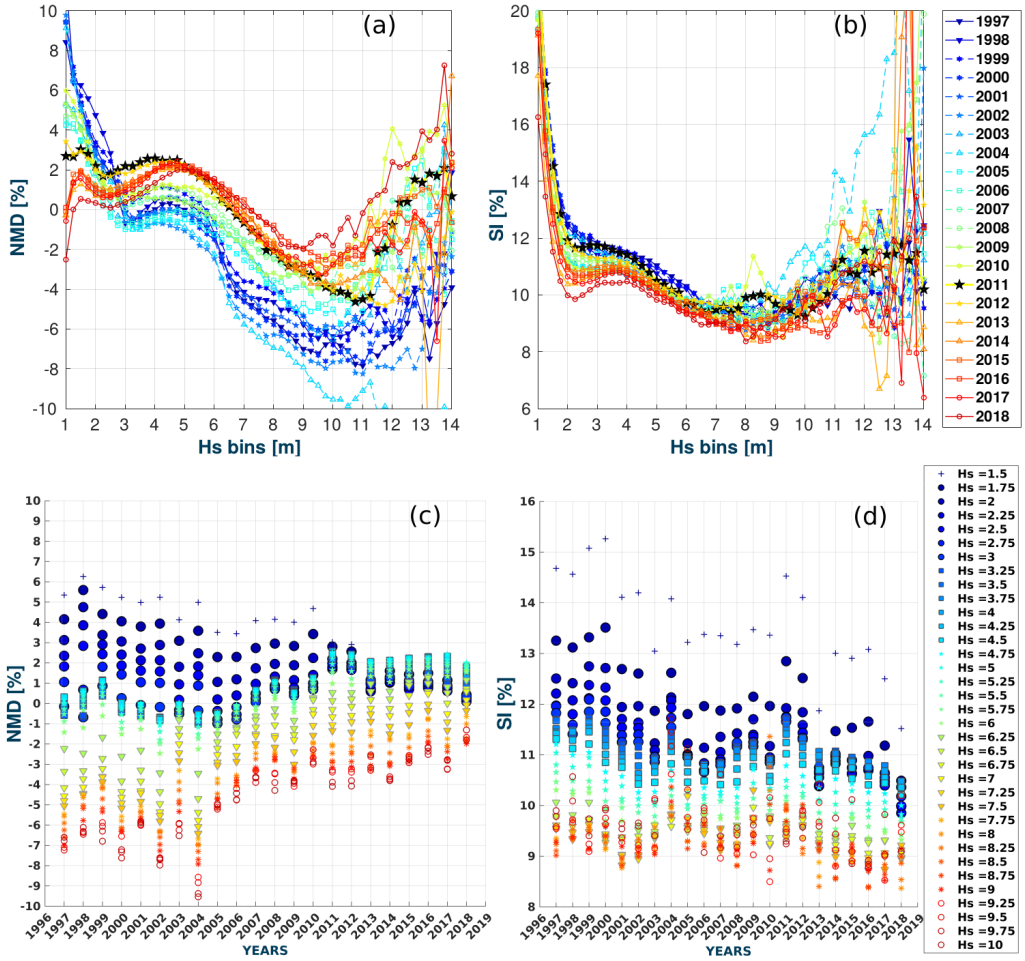

Figure 20: Performance parameters for 22 years hindcast using T475. (a) H_s NMD curves and (b) SI curves, the reference year (2011) used for model tuning has been highlighted with a black star. (c) and (d) are the NMD and SI time series of 1.5 to 10 m H_s bins. Bin size is 0.25 m. Altimeters used for validation: Topex (1997-2002), Envisat (2003-2010), Jason-2 (2011-2012), Saral (2013-2018).

6.2. Comparison to ERA5 wave heights

Because the ERA5 reanalysis also included a wave model it is questionable that our efforts have any added value, especially because the ERA5 wave model assimilates altimeter wave heights and uses a wind forcing at the 10 minutes time step of the atmospheric circulation model to which it is coupled. However, we know (J.R. Bidlot, personal communication) that the same

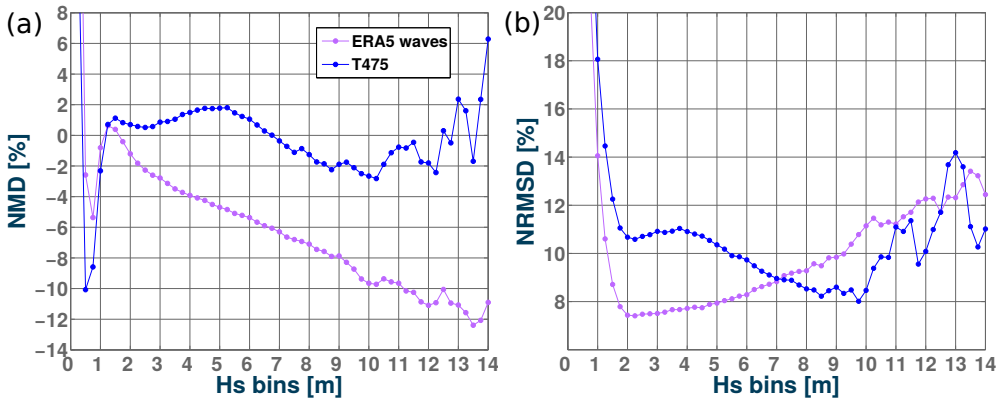

Figure 21: Performance parameters curves for test T475 and ERA5 wave product with respect to Jason-3 altimeter data. (a) H_s NMD, and (b) NRMSD. Analyzed year: 2018. H_s bin size is 0.25 m.

ECMWF wave model that uses improved wave generation and dissipation parameterization in the IFS cycle 46R1 that is operational as of June 6, 2019 (ECMWF, 2019) and is similar to T471, already gives better results than the ERA5 wave heights at buoy locations. It is thus interesting to look at the differences between the ERA5 wave heights and the results of the present hindcast. We note that our model uses different forcing, in particular for currents, sea ice and icebergs, includes some shoreline and iceberg reflexion and produces different output parameters, including fluxes of energy between the ocean and atmosphere, in addition to the parameters that can be derived from the wave spectrum. Here we only compare the two simulations using the Jason-3 data for 2018, which has not been assimilated in ERA5.

Fig. 21 shows a very strong negative bias in the ERA5 wave heights that, combined with a much lower random errors, gives larger rms differences for $H_s > 7$ m. Looking at the spatial distribution of these errors we typically find larger random errors in the Southern ocean with T475 compared to ERA5 wave heights (Fig. 22), possibly a benefit of the assimilation of the other satellite missions where the satellite tracks are most dense, and we find lower random error in a few specific areas with T475, including in the Agulhas current, which shows again the benefit of properly including ocean surface currents in a wave model.

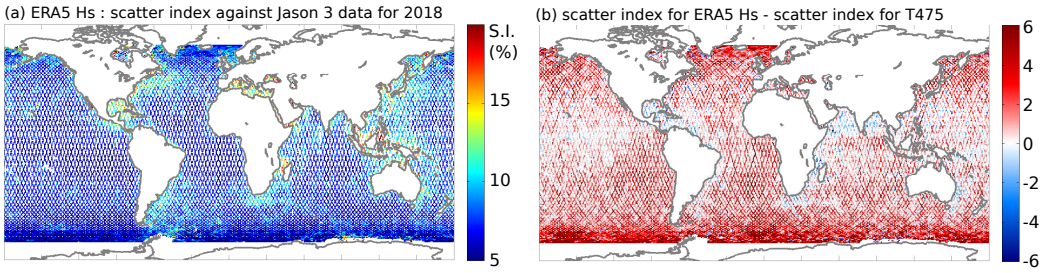

Figure 22: (a) Scatter Index for 1 year (2018) averaged ERA-5 H_s with respect to Jason-3 altimeter data. (b) Difference in scatter index between T475 and ERA-5 waves product.

6.3. Validation with buoy data

So far all of our analysis, except for a brief discussion of mean direction and directional spread, has been based on wave heights alone, whereas our model hindcast is based on the simulation of ocean wave spectra and produces a wide range of spatially gridded parameters as well as spectra at selected locations: around 10,000 points all along the world coastline plus the locations of moored buoys and a few additional offshore points. Even though the model was only marginally changed compared to the version validated by Stopa et al. (2016a), it is interesting to look at errors on the shape of spectra and wave period and directions parameters.

These comparisons are not simple because of the large response differences of different buoy types for wavelengths shorter than 10 m ($f \simeq 0.4$ Hz) in particular 3 m diameter discus buoys tend to filter frequencies above 0.4 Hz which are well reproduced, up to 0.6 Hz by 0.8 m diameter Waverider buoys (e.g. Ardhuin et al., 2019). We thus focus on the 0.05 to 0.4 Hz frequency band. Another difficulty is that most Waverider buoys are located in coastal areas. We have particularly selected 5 buoys that are representative of different wave climates, as listed in Table 4. The buoy heave spectra were averaged over 3 h intervals.

Fig. 23 shows different validations of the spectral content of the wave spectrum. Away from the coasts, at station Papa (buoy 46246), the average wave spectra in Fig. 23.a reveal a general good behavior of the model compared to Datawell buoy measurements with mean differences under 10% in the frequency range 0.05 to 0.4 Hz. The deviation at low frequencies can be due to the presence of infragravity waves in the buoy measurements which were not included in our model simulation, but could have been added and have a typical height of 1 cm in the open ocean (Ardhuin et al., 2014). That

WMO code	latitude	longitude	depth	shore distance	buoy type
46246	50.0N	145.2 W	4252 m	900 km	Datawell WR
51208	22.285 N	159.574 W	200 m	5 km	Datawell WR
51004	17.53 N	152.25 W	5183 m	300 km	3-m discus
42097	25.7 N	83.65 W	81 m	130 km	Datawell WR
44098	42.8 N	70.17 W	77 m	37 km	Datawell WR

Table 4: List of buoys selected for detailed validation over the years 2018 and 2019. Note that data was missing before July 6, 2019 for buoy 46246.

deviation could also be the result of mooring line effects. At high frequencies, the model understimation for $f > 0.5$ Hz may be due to the buoy heave resonance (Datawell, 2014).

The variability of the energy content at different frequencies is generally well captured by the parameters H_s and mean periods $T_{m0,2}$ (which is more sensitive to the high frequencies) and $T_{m-1,0}$ (more sensitive to the low frequencies). With a bias for the mean periods at buoy 46246 under 1% and a scatter index around 5%, the model is particularly accurate for the shape of the wave spectrum.

For other buoys, differences between the model and the observations can reveal errors in buoy measurements (e.g. the spectrum roll-off for $f > 0.52$ Hz at 51004 is typical of 3-m discus buoys) and difficulties for the model to resolve coastal sea state variability and growth for relatively short fetches. In particular, the energy for low frequencies ($f < 0.06$ Hz) is strongly underestimated in the Gulf of Mexico and the Gulf of Maine.

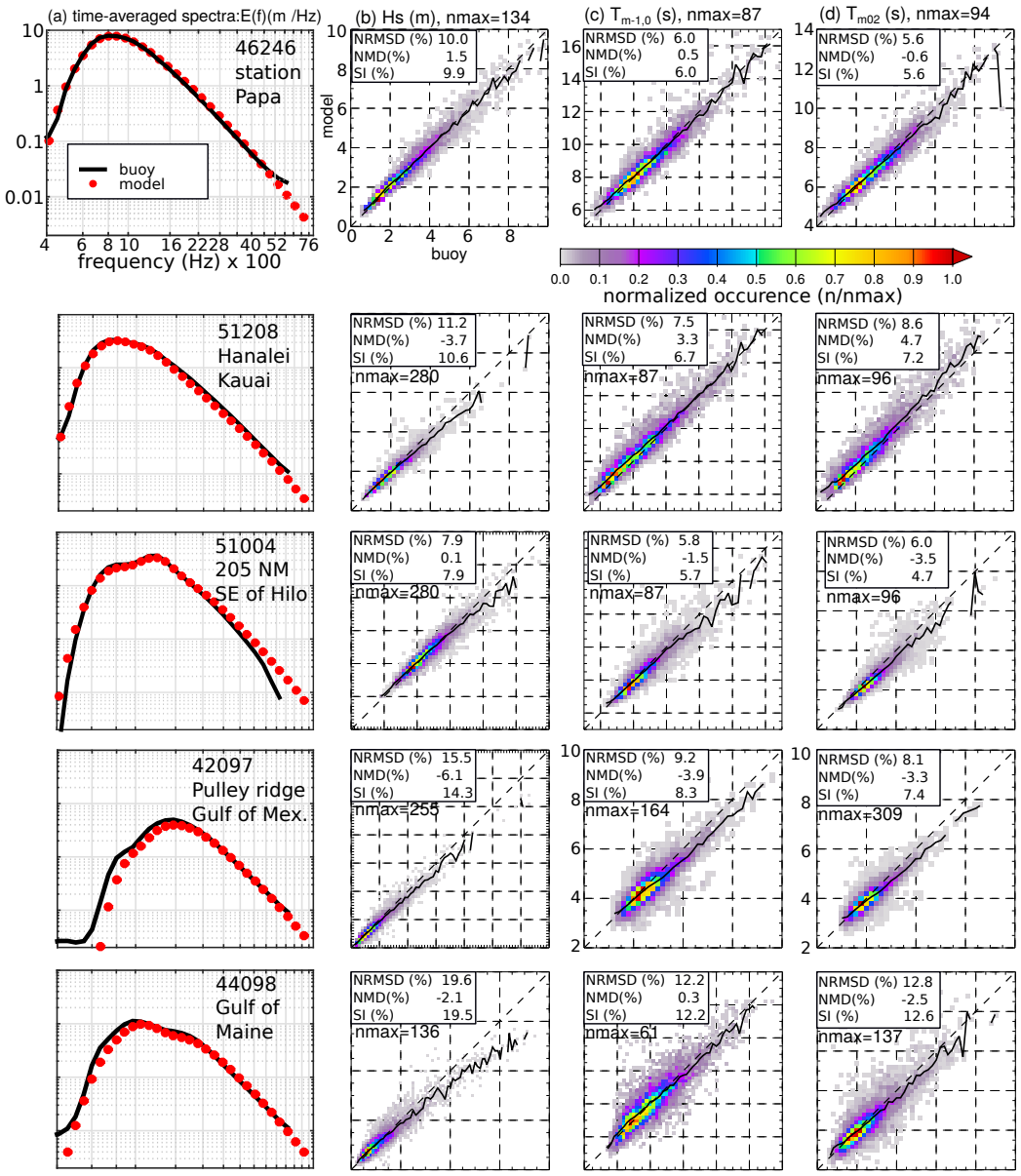

Figure 23: Modeled and measured mean spectra, scatter plots for H_s, and mean periods $T_{m-1,0}$, $T_{m0,2}$ at selected buoys listed in Table 4.

7. Conclusions

The present paper discusses the influence of forcing fields (winds, surface current, sea ice concentration, iceberg concentration), parameterizations (wind-wave generation and swell damping) and resolution (in physical and spectral space) on the wave heights produced by a wave model hindcast, using the WAVEWATCH III modelling framework and satellite-derived wave heights. It is unfortunately not practical to test all the possible combinations of model settings, but we expect that the choice of forcing fields and adjustment of parameters is generally robust, and the measurements shows that the present hindcast, in the context of the Integrated Ocean Waves for Geophysical and other Applications (IOWAGA) project, is generally superior to the previous version described by Rascle and Ardhuin (2013), and in some regions, for large wave heights, is superior to the ERA5 reanalysis wave product.

For the forcing, we found that ERA5 winds, once corrected for a low bias at wind speeds above 21 m/s, gave more accurate results than operational ECMWF analyses or the CFSR reanalysis. Alternative merged satellite-model products (Bentamy et al., 2018) gave interesting results. We also found that the use of currents provided by CMEMS-Globcurrent generally improved the model results. Probably because these current estimates are missing a significant part of the Total Surface Current Velocity, they degraded the model results at latitudes larger than 50° N. Finally, we confirmed the importance of both sea ice and icebergs for Southern Ocean and Arctic wave heights.

For the model parameterizations of air-sea interactions, we have shown that the distribution of H_s around the global maximum of 2 m, could be used to adjust the transition from a laminar to a turbulent boundary layers above the waves, that is very important for the attenuation of swells, and is probably the most sensitive part of the model parameterizations.

Regarding model discretizations, we have found a great benefit in including the 0.7 to 1 Hz frequency range, even though the directionality in that range is not yet well described by the model when waves are developed.

For all these tests, we have only performed limited validation for other parameters besides the significant wave height. We expect that future adjustments will particularly focus on the high frequencies ($f > 0.4$ Hz) with more validation of the variables that are most sensitive to that frequency range, starting with the mean square slope and its directional components. In this

respect, we expect to produce a Part 4 update on the present work based on the parameterizations of Romero (2019) and a much better treatment of the model high frequencies that would make it consistent with remote sensing data, as analyzed by Nouguier et al. (2016) or Yueh et al. (2006), following the work of Elfouhaily et al. (1997).

Acknowledgments

The present work was supported by ESA Climate Change Initiative Program, EU ERANET Resourcecode and CNES. Buoy data were furnished by the Coastal Data Information Program (CDIP), Integrative Oceanography Division, operated by the Scripps Institution of Oceanography, under the sponsorship of the U.S. Army Corps of Engineers and the California Department of Parks and Recreation. https://doi.org/10.18437/C7WC72. We are grateful to many colleagues, including Abderrahim Bentamy and Camille Lique for many constructive discussions. The authors would like to thank to the 4 anonymous reviewers who, through their comments and observations, have helped to improve the quality of this manuscript.

Data availability

The generated hindcast using test T475, will be available in the following web site: https://www.umr-lops.fr/Donnees/Vagues/sextant

At the moment of the generation of the present study, the wave data set covers 28 years, from 1993 to 2020 with 3-hourly outputted data. The extension of the hindcast to prior and more recent years is an ongoing work.

Appendix A. Detailed model implementation

The wave model hindcast and tests presented here all use version 7.0 of WAVEWATCH III. The hindcast uses a list of switches, which appears in all NetCDF file products,

- physical parameterizations : LN1 ST4 STAB0 NL1 BT4 DB1 MLIM TR0 BS0 IC2 IS2 REF1 RWND WCOR
- advection and GSE correction: PR3 UQ

- other numerical aspects: F90 NOGRB NC4 SCRIP SCRIPNC DIST MPI FLX0 XX0 WNT2 WNX1 CRT1 CRX1 TIDE TRKNC O0 O1 O2 O2a O2b O2c O3 O4 O5 O6 O7

The model parameters are adjusted with the same parameters for all model grids, and except for default parameter values the T475 parameters use these adjustments

- air-sea interaction parameters (SIN4 namelist) BETAMAX = 1.75, SWELLF = 0.66, TAUWSHELTER = 0.3, SWELLF3 = 0.022, SWELLF4 = 115000.0, SWELLF7 = 432000.00

- wave-ice dissipation parameters (SIC2 namelist) IC2DISPER = F, IC2TURB = 1.0, IC2ROUGH = 0.001, IC2DMAX = 0.3, IC2REYNOLDS = 150000, IC2SMOOTH = 200000., IC2VISC = 2.

- wave-ice scattering and floe size effects including break-up and inelastic dissipation (SIS2 namelist): ISC1 = 0.2, IS2C2 = 0., IS2C3 = 0., IS2BACKSCAT = 1., IS2BREAK = T, IS2DUPDATE = F, IS2CREEPB = 0.2E8, IS2CREEPD = 0.5, IS2CREEPN = 3.0, IS2BREAKF = 3.6, IS2WIM1 = 1.0, IS2FLEXSTR = 2.7414E+05, IS2CREEPC = 0.4, IS2ANDISE = 0.55

- reflexion parameters (REF1 namelist): REFCOAST = 0.05, REFCOSP_STRAIGHT = 4, REFFREQ = 1., REFICEBERG = 0.2, REFMAP = 0., REFSLOPE=0., REFSUBGRID = 0.1, REFRMAX = 0.5

- other parameterizations (MISC namelist) ICEHINIT = 1., ICEHMIN = 0.1, CICE0 = 0.25, CICEN = 2.00, LICE = 40000., FLAGTR = 4, FACBERG = 0.2, NOSW = 6, WCOR1 = 21., WCOR2 = 1.05 /

- activation of 3D output fields (full spectra and seismic sources, OUTS namelist) P2SF = 1, E3D = 1, I1P2SF = 3, I2P2SF = 24

References

Ardhuin, F., Chapron, B., Collard, F., 2009. Observation of swell dissipation across oceans. Geophys. Res. Lett. 36, L06607.

767 Ardhuin, F., Dumas, F., Bennis, A.-C., Roland, A., Sentchev, A., Forget,
768 P., Wolf, J., Girard, F., Osuna, P., Benoit, M., 2012. Numerical wave
769 modeling in conditions with strong currents: dissipation, refraction and
770 relative wind. J. Phys. Oceanogr. 42, 2101–2120.

771 Ardhuin, F., Herbers, T. H. C., 2005. Numerical and physical diffusion: Can
772 wave prediction models resolve directional spread? J. Atmos. Ocean Tech-
773 nol. 22 (7), 886–895.
774 URL http://journals.ametsoc.org/doi/pdf/10.1175/JTECH1723.1

775 Ardhuin, F., Otero, M., Merrifield, S., Grouazel, A., Terrill, E., 2020. Ice
776 breakup controls dissipation of wind waves across southern ocean sea ice.
777 Geophys. Res. Lett. 47, e2020GL087699.

778 Ardhuin, F., Rascle, N., Chapron, B., Gula, J., Molemaker, J., Gille, S. T.,
779 Menemenlis, D., Rocha, C., 2017a. Small scale currents have large effects
780 on wind wave heights. J. Geophys. Res. 122 (C6), 4500–4517.

781 Ardhuin, F., Rawat, A., Aucan, J., 2014. A numerical model for free in-
782 fragravity waves: Definition and validation at regional and global scales.
783 Ocean Modelling 77, 20–32.

784 Ardhuin, F., Rogers, E., Babanin, A., Filipot, J.-F., Magne, R., Roland, A.,
785 van der Westhuysen, A., Queffeulou, P., Lefevre, J.-M., Aouf, L., Collard,
786 F., 2010. Semi-empirical dissipation source functions for wind-wave models:
787 part I, definition, calibration and validation. J. Phys. Oceanogr. 40 (9),
788 1917–1941.

789 Ardhuin, F., Roland, A., 2012. Coastal wave reflection, directional spreading,
790 and seismo-acoustic noise sources. J. Geophys. Res. 117, C00J20.

791 Ardhuin, F., Stopa, J. E., Chapron, B., Collard, F., Husson, R., Jensen,
792 R. E., Johannessen, J., Mouche, A., Passaro, M., Quartly, G. D., Swail,
793 V., Young, I., 2019. Observing sea states. Frontiers in Marine Sci. 6, 124.

794 Ardhuin, F., Suzuki, N., McWilliams, J. C., Aiki, N., 2017b. Comments on
795 "a combined derivation of the integrated and vertically resolved, coupled
796 wave-current equations". J. Phys. Oceanogr. 47 (9), 2377–2385.

797 Ardhuin, F., Tournadre, J., Queffelou, P., Girard-Ardhuin, F., 2011. Obser-
798 vation and parameterization of small icebergs: drifting breakwaters in the
799 southern ocean. Ocean Modelling 39, 405–410.

800 Ballarotta, M., Ubelmann, C., Pujol, M.-I., Taburet, G., Fournier, F., Leg-
801 eais, J.-F., Faugere, Y., Delepoulle, A., Chelton, D., Dibarboure, G., Picot,
802 N., 2019. On the resolutions of ocean altimetry maps. Ocean Science Dis-
803 cussions .

804 Banner, M. L., Morison, R. P., 2006. On modeling spectral dissipation due
805 to wave breaking for ocean wind waves. In: Proceedings of the 9th Inter-
806 national workshop on wave hindcasting and forecasting, Victoria, Canada.

807 Banner, M. L., Young, I. R., 1994. Modeling spectral dissipation in the
808 evolution of wind waves. part I: assessment of existing model performance.
809 J. Phys. Oceanogr. 24 (7), 1550–1570.
810 URL http://ams.allenpress.com/archive/1520-0485/24/7/pdf/
811 i1520-0485-24-7-1550.pdf

812 Barrick, D. E., Headrick, J. M., Bogle, R. W., Crombie, D. D., 1974. Sea
813 backscatter at HF: interpretation and utilization of the echo. Proc. IEEE
814 62, 673.

815 Bentamy, A., Grodsky, S. A., Carton, J. A., Croizé-Fillon, D., Chapron, B.,
816 2012. The era-interim reanalysis: configuration and performance of the
817 data assimilation system. J. Geophys. Res. 117, C02011.

818 Bentamy, A., Grodsky, S. A., Chapron, B., Carton, J. A., 2013. Compatibility
819 of C- and Ku-band scatterometer winds: ERS-2 and QuikSCAT. J. Mar.
820 Sys. 117–118, 72–80.

821 Bentamy, A., Piollé, J. F., Prevost, C., 2018. Product user manual for wind
822 product WIND_GLO_WIND_L4_REP_OBSERVATIONS_012_006. Tech.
823 Rep. CMEMS-WIND-PUM-012-006, EU Copernicus Marine Service.

824 Bidlot, J., 2005. Use of Mercator surface currents in the ECMWF forecasting
825 system. Tech. Rep. Memorandum R60.9/JB/10104, Research Department,
826 ECMWF, Reading, U. K.

827 Bidlot, J., Janssen, P., Abdalla, S., 2005. A revised formulation for ocean
828 wave dissipation in CY25R1. Tech. Rep. Memorandum R60.9/JB/0516,
829 Research Department, ECMWF, Reading, U. K.

830 Bidlot, J., Janssen, P., Abdalla, S., 2007. A revised formulation of ocean wave
831 dissipation and its model impact. Tech. Rep. Memorandum 509, ECMWF,
832 Reading, U. K.

833 Boudière, E., Maisondieu, C., Ardhuin, F., Accensi, M., Pineau-Guillou, L.,
834 Lepesqueur, J., 2013. A suitable metocean hindcast database for the design
835 of marine energy converters. Int. J. Mar. Energy 28 (3–4), e40–e52.

836 Boutin, G., Ardhuin, F., Dumont, D., Sévigny, C., Girard-Ardhuin, F., 2018.
837 Floe size effects on wave-ice interactions: theoretical background, imple-
838 mentation and applications. J. Geophys. Res. 123, 4779–4805.

839 Cavaleri, L., Bertotti, L., 1997. In search of the correct wind and wave fields
840 in a minor basin. Mon. Weather Rev. 125 (8), 1964–1975.
841 URL http://ams.allenpress.com/archive/1520-0493/125/11/pdf/
842 i1520-0493-125-8-1964.pdf

843 Chawla, A., Tolman, H. L., 2008. Obstruction grids for spectral wave models.
844 Ocean Modelling 22, 12–25.

845 Chawla, A., Tolman, H. L., Gerald, V., Spindler, D., Spindler, T., Alves,
846 J.-H. G. M., Cao, D., Hanson, J. L., Devaliere, E.-M., 2013. A multigrid
847 wave forecasting model: A new paradigm in operational wave forecasting.
848 Weather and Forecasting 28, 1057–1078.

849 Chen, G., Belcher, S. E., 2000. Effects of long waves on wind-generated waves.
850 J. Phys. Oceanogr. 30, 2246–2256.
851 URL http://tinyurl.com/38cbjnk

852 Chen, G., Chapron, B., Ezraty, R., Vandemark, D., 2002. A global view of
853 swell and wind sea climate in the ocean by satellite altimeter and scat-
854 terometer. J. Atmos. Ocean Technol. 19, 1849–1859.

855 Datawell, 2014. Datawell - high frequency heave resonance. Tech. Rep. see
856 https://www.youtube.com/watch?v=OlrCKTnrhbQ.
857 URL https://www.youtube.com/watch?v=OlrCKTnrhbQ

De Carlo, M., Ardhuin, F., Pichon, A. L., 2020. Atmospheric infrasound radiation from ocean waves in finite depth: a unified generation theory and application to radiation patterns. Geophys. J. Int. 221, 569–585.

De Carlo, M., Hupe, P., Le Pichon, A., Ardhuin, F., 2021. Global microbarom patterns: a first confirmation of the theory for source and propagation. Geophys. Res. Lett. in press.

Dee, D. P., Uppala, S. M., Simmons, A. J., Berrisford, P., Poli, P., Kobayashi, S., Andrae, U., Balmaseda, M. A., Balsamo, G., Bauer, P., Bechtold, P., Beljaars, A. C. M., van de Berg, L., Bidlot, J., Bormann, N., Delsol, C., Dragani, R., Fuentes, M., Geer, A. J., Haimbergere, L., Healy, S. B., Hersbach, H., Holm, E. V., Isaksena, L., Køallberg, P., Köhler, M., Matricardi, M., McNally, A. P., Monge-Sanz, B. M., Morcrette, J.-J., Park, B.-K., Peubey, C., de Rosnay, P., Tavolato, C., Thépaut, J.-N., Vitart, F., 2011. The era-interim reanalysis: configuration and performance of the data assimilation system. Quart. Journ. Roy. Meteorol. Soc. 137, 553–597.

Doble, M. J., Bidlot, J.-R., 2013. Wave buoy measurements at the Antarctic sea ice edge compared with an enhanced ECMWF WAM: Progress towards global waves-in-ice modelling. Ocean Modelling 70, 166–173.

Doble, M. J., Coon, M. D., Wadhams, P., 2003. Pancake ice formation in the weddell sea. J. Geophys. Res. 108 (C7), 3209.

Dobler, D., Huck, T., Maes, C., Grima, N., Blanke, B., Martinez, E., Ardhuin, F., 2019. Large impact of stokes drift on the fate of surface floating debris in the south indian basin 148, 202–209.

Dodet, G., Piolle, J.-F., Quilfen, Y., Abdalla, S., Accensi, M., Ardhuin, F., Ash, E., Bidlot, J.-R., Gommenginger, C., Marechal, G., Passaro, M., Quartly, G., Stopa, J., Timmermans, B., Young, I., Cipollini, P., Donlon, C., 2020. The sea state cci dataset v1: towards a sea state climate data record based on satellite observations. Earth System Sci. Data 12, 1929–1951.

ECMWF, 2019. IFS Documentation CY46R1, Part VII: ECMWF Wave Model. Tech. Rep. 333, ECMWF, Reading, UK, 103 pp.
URL https://www.ecmwf.int/node/19311

Elfouhaily, T., Chapron, B., Katsaros, K., Vandemark, D., 1997. A unified directional spectrum for long and short wind-driven waves. J. Geophys. Res. 102 (C7), 15781–15796.

Elipot, S., Lumpkin, R., Perez, R. C., Lilly, J. M., Early, J. J., Sykulski, A. M., 2016. A global surface drifter data set at hourly resolution. J. Geophys. Res. 121, 2937–2966.

ESA, May 2019. Report for mission selection: SKIM. Tech. Rep. ESA-EOPSM-SKIM-RP-3550, European Space Agency, Noordwijk, The Netherlands.

Farrell, W. E., Munk, W., 2010. Booms and busts in the deep. J. Phys. Oceanogr. 40 (9), 2159–2169.

Fraser, C. I., Morrison, A. K., Hogg, A. M., Macaya, E. C., van Sebille, E., Ryan, P. G., Padovan, A., Jack, C., Valdivia, N., Waters, J. M., 2018. Antarctica's ecological isolation will be broken by storm-driven dispersal and warming. Nature Climate Change 8, 704–708.

Gelaro, R., McCarty, W., Suárez, M. J., Todling, R., Molod, A., Takacs, L., Randles, C. A., Darmenov, A., Bosilovich, M. G., Reichle, R., et al., 2017. The modern-era retrospective analysis for research and applications, version 2 (merra-2). Journal of climate 30 (14), 5419–5454.

Girard-Ardhuin, F., Ezraty, R., 2012. Enhanced arctic sea ice drift estimation merging radiometer and scatterometer data. IEEE Trans. on Geosci. and Remote Sensing 50, 2639–2648.

Hanafin, J., Quilfen, Y., Ardhuin, F., Sienkiewicz, J., Queffeulou, P., Obrebski, M., Chapron, B., Reul, N., Collard, F., Corman, D., de Azevedo, E. B., Vandemark, D., Stutzmann, E., 2012. Phenomenal sea states and swell radiation: a comprehensive analysis of the 12-16 February 2011 North Atlantic storms. Bull. Amer. Meterol. Soc. 93, 1825–1832.

Hasselmann, S., Hasselmann, K., 1985. Computation and parameterizations of the nonlinear energy transfer in a gravity-wave spectrum. part I: a new method for efficient computations of the exact nonlinear transfer. J. Phys. Oceanogr. 15, 1369–1377.

Hersbach, H., Bell, B., Berrisford, P., Hirahara, S., Horányi, A., Muñoz-Sabater, J., Nicolas, J., Peubey, C., Radu, R., Schepers, D., Simmons, A., Soci, C., Abdalla, S., Abellan, X., Balsamo, G., Bechtold, P., Biavati, G., Bidlot, J., Bonavita, M., Chiara, G. D., Dahlgren, P., Dee, D., Diamantakis, M., Dragani, R., Flemming, J., Forbes, R., Fuentes, M., Geer, A., Haimberger, L., Healy, S., Hogan, R. J., Hólm, E., Janisková, M., Keeley, S., Laloyaux, P., Lopez, P., Lupu, C., Radnoti, G., de Rosnay, P., Rozum, I., Vamborg, F., Villaume, S., Thépaut, J., 2020. The ERA5 global reanalysis. Quart. Journ. Roy. Meteorol. Soc. 146, 1999–2049.

Hersbach, H., Bidlot, J. R., 2008. The relevance of ocean surface current in the ECMWF analysis and forecast system. In: Proceedings from the ECMWF Workshop on Atmosphere-Ocean Interaction, 10-12 November 2008. ASCE.
URL www.ecmwf.int/publications/library/do/references/list/28022009

Janssen, P. A. E. M., 1991. Quasi-linear theory of wind wave generation applied to wave forecasting. J. Phys. Oceanogr. 21, 1631–1642, see comments by D. Chalikov, J. Phys. Oceanogr. 1993, vol. 23 pp. 1597–1600.
URL http://journals.ametsoc.org/doi/pdf/10.1175/1520-0485%281991%29021%3C1631%3AQLTOWW%3E2.0.CO%3B2

Kuik, A. J., van Vledder, G. P., Holthuijsen, L. H., 1988. A method for the routine analysis of pitch-and-roll buoy wave data. J. Phys. Oceanogr. 18, 1020–1034.
URL http://journals.ametsoc.org/doi/pdf/10.1175/1520-0485%281987%29017%3C0845%3ATROWDT%3E2.0.CO%3B2

Leckler, F., 2013. Observation et modélisation du déferlement des vagues. Ph.D. thesis, Université Européenne de Bretagne, Ecole doctorale des Sciences de la Mer, Brest, France.
URL http://tinyurl.com/leckler-thesis

Leckler, F., Ardhuin, F., Filipot, J.-F., Mironov, A., 2013. Dissipation source terms and whitecap statistics. Ocean Modelling 70 (9), 62–74.

Lecocq, T., Ardhuin, F., Collin, F., Camelbeeck, T., 2019. On the extraction of microseismic groundmotion from analog seismograms for the validation of ocean-climate models. Seismol. Res. Lett. 91, 1518–1530.

Leonard, B. P., 1991. The ULTIMATE conservative difference scheme applied to unsteady one-dimensional advection. Computational Methods in Applied Mechanical Engineering 88, 17–74.

Lumpkin, R., Özgökmen, T., Centurioni, L., 2017. Advances in the application of surface drifters. Annu. Rev. Mar. Sci. 9, 6.1–6.23.

Marechal, G., Ardhuin, F., 2020. Surface currents and significant wave height gradients: matching numerical models and high-resolution altimeter wave heights in the agulhas current region. J. Geophys. Res. in press.

Mentaschi, L., Besio, G., Cassola, F., Mazzino, A., 2015. Performance evaluation of WAVEWATCH III in the mediterranean sea. Ocean Modelling 90, 82–94.

Mulet, S., Rio, M.-H., Etienne, H., Artana, C., Cancet, M., Dibarboure, G., Feng, H., Husson, R., Picot, N., Provost, C., et al., 2021. The new cnes-cls18 global mean dynamic topography. Ocean Science Discussions , 1–31.

Munk, W., 2009. An inconvenient sea truth: Spread, steepness, and skewness of surface slopes. Annu. Rev. Mar. Sci. 1, 377–415.

Nishida, K., Takagi, R., 2016. Teleseismic S wave microseisms. Science 353, 919–921.

Nouguier, F., Mouche, A., Rascle, N., Chapron, B., Vandemark, D., 2016. Analysis of dual-frequency ocean backscatter measurements at Ku- and Ka-bands using near-nadir incidence GPM radar data. IEEE Geoscience And Remote Sensing Letters 31, 2023–2245.

Onink, V., Wichmann, D., Delandmeter, P., van Sebille, E., Mar. 2019. The role of Ekman currents, geostrophy and Stokes drift in the accumulation of floating microplastic . J. Geophys. Res. 124, 1474–1490.

Perignon, Y., Ardhuin, F., Cathelain, M., Robert, M., 2014. Swell dissipation by induced atmospheric shear stress. J. Geophys. Res. 119, 6622–6630.

Peureux, C., Ardhuin, F., 2016. Ocean bottom pressure records from the cascadia array and short surface gravity waves. J. Geophys. Res. 121, 2862–2873.

Peureux, C., Ardhuin, F., Guimaraes, P. V., 2020. On the unsteady steepening of short gravity waves near the crests of longer waves in the absence of generation or dissipation. J. Geophys. Res. .

Peureux, C., Benetazzo, A., Ardhuin, F., 2018. Note on the directional properties of meter-scale gravity waves. Ocean Science 14, 41–52.

Phillips, O. M., 1985. Spectral and statistical properties of the equilibrium range in wind-generated gravity waves. J. Fluid Mech. 156, 505–531.

Pineau-Guillou, L., Ardhuin, F., Bouin, M.-N., Redelsperger, J.-L., Chapron, B., Bidlot, J., Quilfen, Y., 2018. Strong winds in a coupled wave-atmosphere model during a north Atlantic storm event: evaluation against observations. Quart. Journ. Roy. Meteorol. Soc. 144, 317–332.

Quilfen, Y., Chapron, B., 2019. Ocean surface wave-current signatures from satellite altimeter measurements. Geophys. Res. Lett. 216, 253–261.

Quilfen, Y., Chapron, B., Vandemark, D., 2004. The ERS scatterometer wind measurement accuracy: evidence of seasonal and regional biases. J. Atmos. Ocean Technol. 18, 1684–1697.
URL http://ams.allenpress.com/archive/1520-0426/18/10/pdf/i1520-0426-18-10-1684.pdf

Rapizo, H., Durrant, T. H., Babanin, A. V., 2018. Current-induced dissipation in spectral wave models. Ocean Dynamics 68, 939–955.

Rascle, N., Ardhuin, F., 2013. A global wave parameter database for geophysical applications. part 2: model validation with improved source term parameterization. Ocean Modelling 70, 174–188.

Rascle, N., Ardhuin, F., Queffeulou, P., Croizé-Fillon, D., 2008. A global wave parameter database for geophysical applications. part 1: wave-current-turbulence interaction parameters for the open ocean based on traditional parameterizations. Ocean Modelling 25, 154–171.
URL http://hal.archives-ouvertes.fr/hal-00201380/

Renault, L., Molemaker, M. J., McWilliams, J. C., Shchepetkin, A. F., Lemarié, F., Chelton, D., Illig, S., Hall, A., 2016. Modulation of wind work by oceanic current interaction with the atmosphere. J. Phys. Oceanogr. 46, 1685–1704.

1018 Retailleau, L., Boué, P., Stehly, L., Campillo, M., 2017. Locating microseism
1019 sources using spurious arrivals in intercontinental noise correlations. J.
1020 Geophys. Res. 122, 8107–8120.

1021 Rio, M.-H., Mulet, S., Picot, N., 2014. Beyond GOCE for the ocean circu-
1022 lation estimate: Synergetic use of altimetry, gravimetry, and in situ data
1023 provides new insight into geostrophic and Ekman currents. Geophys. Res.
1024 Lett. 41, 8918–8925.

1025 Rivas, M. B., Stoffelen, A., 2019. Characterizing ERA-Interim and ERA5
1026 surface wind biases using ASCAT. Ocean Sci. 15, 831–852.

1027 Roarty, H., Cook, T., Hazard, L., George, D., Harlan, J., Cosoli, S., Wyatt,
1028 L., Fanjul, E. A., Terrill, E., Otero, M., Largier, J., Glenn, S., Ebuchi, N.,
1029 Whitehouse, B., Bartlett, K., Mader, J., Rubio, A., Corgnati, L., Man-
1030 tovani, C., Griffa, A., Reyes, E., Lorente, P., Flores-Vidal, X., Saavedra-
1031 Matta, K. J., Rogowski, P., Prukpitikul, S., Lee, S.-H., Lai, J.-W., Guerin,
1032 C.-A., Sanchez, J., Hansen, B., Grilli, S., 2019. The global high frequency
1033 radar network. Frontiers in Marine Sci. 6, 164:1–164:23.

1034 Roland, A., Ardhuin, F., 2014. On the developments of spectral wave models:
1035 numerics and parameterizations for the coastal ocean. Ocean Dynamics
1036 64 (6), 833–846.

1037 Romero, L., 2019. Distribution of surface wave breaking fronts. Geophys.
1038 Res. Lett. 46, 10463–10474.

1039 Romero, L., Lenain, L., Melville, W. K., 2017. Observations of surface wave–
1040 current interaction. J. Phys. Oceanogr. 47, 615–632.

1041 Saha, S., Moorthi, S., Pan, H.-L., Wu, X., Wang, J., Nadiga, S., Tripp, P.,
1042 Kistler, R., Woollen, J., Behringer, D., Liu, H., Stokes, D., Grumbine, R.,
1043 Gayno, G., Wang, J., Hou, Y.-T., ya Chuang, H., Juang, H.-M. H. a. J. S.,
1044 Iredell, M., Treadon, R., Kleist, D., Delst, P. V., Keyser, D., Derber, J.,
1045 Ek, M., Meng, J., Wei, H., Yang, R., Lord, S., van den Dool, H., Kumar,
1046 A., Wang, W., Long, C., Chelliah, M., Xue, Y., Huang, B., Schemm, J.-K.,
1047 Ebisuzaki, W., Lin, R., Xie, P., Chen, M., Zhou, S., Higgins, W., Zou, C.-
1048 Z., Liu, Q., Chen, Y., Han, Y., Cucurull, L., Reynolds, R. W., Rutledge,
1049 G., Goldberg, M., 2010. The NCEP Climate Forecast System Reanalysis.
1050 Bull. Amer. Meterol. Soc. 91, 1015–1057.

1051 Sharmar, V. D., Markina, M. Y., Gulev, S. K., 2021. Global ocean wind-wave
1052 model hindcasts forced by different reanalyzes: A comparative assessment.
1053 J. Geophys. Res. 126.

1054 Smith, W. H. F., Scharroo, R., 2015. Waveform aliasing in satellite radar
1055 altimetry. IEEETGRS 53, 1671–1682.

1056 Stopa, J. E., Ardhuin, F., Bababin, A., Zieger, S., 2016a. Comparison and
1057 validation of physical wave parameterizations in spectral wave models.
1058 Ocean Modelling 103, 2–17.

1059 Stopa, J. E., Ardhuin, F., Girard-Ardhuin, F., 2016b. Wave climate in the
1060 Arctic 1992-2014: seasonality and trends. The Cryosphere 10, 1605–1629.

1061 Stopa, J. E., Ardhuin, F., Stutzmann, E., Lecocq, T., 2019. Sea state trends
1062 and variability: consistency between models, altimeters, buoys, and seismic
1063 data (1979-2016). J. Geophys. Res. 124, in press.

1064 Stutzmann, E., Schimmel, M., Ardhuin, F., 2012. Modeling long-term seismic
1065 noise in various environments. Geophys. J. Int. 191, 707–722.

1066 The WAVEWATCH III ® Development Group, 2019. User manual and sys-
1067 tem documentation of WAVEWATCH III ® version 6.07. Tech. Note 333,
1068 NOAA/NWS/NCEP/MMAB, College Park, MD, USA, 465 pp. + Appen-
1069 dices.

1070 Thomson, J., Ackley, S., Girard-Ardhuin, F., Ardhuin, F., Babanin, A.,
1071 Boutin, G., Brozena, J., Cheng, S., Collins, C., Doble, M., Fairall, C.,
1072 Guest, P., Gebhardt, C., Gemmrich, J., Graber, H. C., Holt, B., Lehner,
1073 S., Lund, B., Meylan, M. H., Maksym, T., Montiel, F., Perrie, W., Persson,
1074 O., Rainville, L., Rogers, W. E., Shen, H., Shen, H., Squire, V., Stammer-
1075 john, S., Stopa, J., Smith, M. M., Sutherland, P., Wadhams, P., 2018.
1076 Overview of the arctic sea state and boundary layer physics program. J.
1077 Geophys. Res. 123.

1078 Thomson, J., D'Asaro, E. A., Cronin, M. F., Rogers, W. E., Harcourt, R. R.,
1079 Shcherbina, A., 2013. Waves and the equilibrium range at ocean weather
1080 station P. J. Geophys. Res. 118, 595–5962.

1081 Tolman, H. L., 1995. On the selection of propagation schemes for a spectral
1082 wind wave model. Office Note 411, NWS/NCEP, 30 pp + figures.

1083 Tolman, H. L., 2002. Alleviating the garden sprinkler effect in wind wave
1084 models. Ocean Modelling 4, 269–289.

1085 Tolman, H. L., 2008. A mosaic approach to wind wave modeling. Ocean
1086 Modelling 25, 35–47.

1087 Tournadre, J., Bouhier, N., Girard-Ardhuin, F., Rémy, F., 2016. Antarctic
1088 iceberg distributions 2002–2010. J. Geophys. Res. 121, 327–349.

1089 Tournadre, J., Poisson, J. C., Steunou, N., Picard, B., 2015. Validation of
1090 AltiKa matching pursuit rain flag. Marine Geodesy 38, 107–1023.

1091 van Vledder, G. P., 2006. The WRT method for the computation of non-linear
1092 four-wave interactions in discrete spectral wave models. Coastal Eng. 53,
1093 223–242.

1094 WAMDI Group, 1988. The WAM model - a third generation ocean wave
1095 prediction model. J. Phys. Oceanogr. 18, 1775–1810.
1096 URL http://journals.ametsoc.org/doi/pdf/10.1175/1520-0485%
1097 281988%29018%3C1775%3ATWMTGO%3E2.0.CO%3B2

1098 Williams, G., Maksym, T., Wilkinson, J., Kunz, C., Murphy, C., Kimball,
1099 P., Singh, H., 2014. Thick and deformed antarctic sea ice mapped with
1100 autonomous underwater vehicles. Nature Geosci. 8, 61–67.

1101 Wunsch, C., Ferrari, R., 2009. Ocean circulation kinetic energy:reservoirs,
1102 sources, and sinks. Annu. Rev. Fluid Mech. 41, 253–282.

1103 Yueh, S. H., Wilson, W. J., Dinardo, S. J., Hsiao, S. V., 2006. Polarimet-
1104 ric microwave wind radiometer model function and retrieval testing for
1105 windsat. IEEE Trans. on Geosci. and Remote Sensing 44 (3), 584–595.